SANDIA REPORT

SAND2006-3002
Unlimited Release
Printed July 2006

Analysis of Cavern Shapes for the Strategic Petroleum Reserve

Steven R. Sobolik and Brian L. Ehgartner

Prepared by
Sandia National Laboratories
Albuquerque, New Mexico 87185 and Livermore, California 94550

Sandia is a multiprogram laboratory operated by Sandia Corporation,
a Lockheed Martin Company, for the United States Department of Energy's
National Nuclear Security Administration under Contract DE-AC04-94AL85000.

Issued by Sandia National Laboratories, operated for the United States Department of Energy by Sandia Corporation.

Available to DOE and DOE contractors from
U.S. Department of Energy
Office of Scientific and Technical Information
P.O. Box 62
Oak Ridge, TN 37831

Telephone: (865) 576-8401
Facsimile: (865) 576-5728
E-Mail: reports@adonis.osti.gov
Online ordering: http://www.osti.gov/bridge

Available to the public from
U.S. Department of Commerce
National Technical Information Service
5285 Port Royal Rd.
Springfield, VA 22161

Telephone: (800) 553-6847
Facsimile: (703) 605-6900
E-Mail: orders@ntis.fedworld.gov
Online order: http://www.ntis.gov/help/ordermethods.asp?loc=7-4-0#online

SAND2006-3002
Unlimited Release
Printed July 2006

Analysis of Cavern Shapes for the Strategic Petroleum Reserve

Steven R. Sobolik and Brian L. Ehgartner
Geoscience and Environment Center
Sandia National Laboratories
P.O. Box 5800
Albuquerque, NM 87185-0751

ABSTRACT

This report presents computational analyses to determine the structural integrity of different salt cavern shapes. Three characteristic shapes for increasing cavern volumes are evaluated and compared to the baseline shape of a cylindrical cavern. Caverns with enlarged tops, bottoms, and mid-sections are modeled. The results address pillar to diameter ratios of some existing caverns in the system and will represent the final shape of other caverns if they are repeatedly drawn down. This deliverable is performed in support of the U.S. Strategic Petroleum Reserve.

Several three-dimensional models using a close-packed arrangement of 19 caverns have been built and analyzed using a simplified symmetry involving a 30-degree wedge portion of the model. This approach has been used previously for West Hackberry (Ehgartner and Sobolik, 2002) and Big Hill (Park et al., 2005) analyses. A stratigraphy based on the Big Hill site has been incorporated into the model. The caverns are modeled without wells and casing to simplify the calculations. These calculations have been made using the power law creep model. The four cavern shapes were evaluated at several different cavern radii against four design factors. These factors included the dilatant damage safety factor in salt, the cavern volume closure, axial well strain in the caprock, and surface subsidence. The relative performance of each of the cavern shapes varies for the different design factors, although it is apparent that the enlarged bottom design provides the worst overall performance. The results of the calculations are put in the context of the history of cavern analyses assuming cylindrical caverns, and how these results affect previous understanding of cavern behavior in a salt dome.

ACKNOWLEDGEMENTS

The authors would like to thank Moo Lee and Darrell Munson for their review and support of this work.

TABLE OF CONTENTS

LIST OF FIGURES

LIST OF TABLES

1. INTRODUCTION

1.1 OBJECTIVE

The U.S. Strategic Petroleum Reserve (SPR) stores crude oil in 62 caverns located at four different sites in Texas (Bryan Mound and Big Hill) and Louisiana (Bayou Choctaw and West Hackberry), as shown in Figure 1. The petroleum is stored in solution-mined caverns in salt dome formations. Each cavern is constructed and then operated using casings inserted through a well bore or well bores that are lined with cemented steel casings from the surface to the top of the cavern.

The SPR sites, as well as most other oil and natural gas storage sites in salt domes along the Gulf Coast, are varied in terms of cavern structure and layout. Some sites, such as the Big Hill site, are characterized by a cavern field of reasonably uniform cavern dimensions (radius, height, shape, and depth) and spacing. Other sites, such as Bayou Choctaw, are characterized by diverse cavern characteristics. Most cavern field designs are based on a pillar-to-diameter (P/D) ratio based on the assumption of cylindrical caverns, and these criteria have served cavern designers well. However, these criteria do not take into account the unusual cavern shapes created either by design, variability in salt properties, or by happenstance.

The calculations presented in this report are based on a three-dimensional model of a close-packed, 19-cavern array, using a solution based on the symmetry of a 30-degree wedge portion of the model. This solution method has been used previously for West Hackberry (Ehgartner and Sobolik, 2002), Big Hill (Park et al., 2005), and cavern integrity testing (Sobolik and Ehgartner, 2006) analyses. A stratigraphy and salt properties defined for the Big Hill site analysis (Park et al., 2005) have been chosen for modeling. The caverns are modeled without wells and casing to simplify the calculations, but predicted ground strains are evaluated at the well locations.

The intent of these calculations is to develop some guidelines to predict cavern performance and damage in salt, utilizing the three-dimensional modeling capabilities of high-performance analytical codes and sophisticated material models. As salt fracturing is known to have occurred at underground storage sites similar to SPR, it is necessary to be able to understand the effects of cavern shape and size on cavern stability, and to be able to predict such behavior under a given set of pressurization and well geometry conditions. There exists little previous work that has investigated the effect of cavern shape on stability. Previous work has been based on two-dimensional studies that do not fully simulate the mechanics of a cavern field; for example, Hugout et al. (1988) evaluated various cylinder height-to-diameter ratios and a double cone shape, and Preece and Wawersik (1984) evaluated several roof shapes and found a flat roof to be superior over spherical and other curved roofs under normal operating conditions.

Four measures of cavern performance are evaluated in this study. The first measure uses safety factors as identified by two separate damage criteria, one being a linear function of the hydrostatic pressure (Van Sambeek et al., 1993), and the other a non-linear model based on laboratory data from samples of Big Hill salt (Lee et al., 2004). The second performance measure looks at cavern volume closure for each characteristic cavern shape. The third measure evaluates

the axial well strain in the caprock above the cavern, and the fourth measure looks at the maximum subsidence at the surface for each cavern design. These measures are compared in terms of both minimum and average P/D ratios, as well as cavern volumes, for different cavern radii.

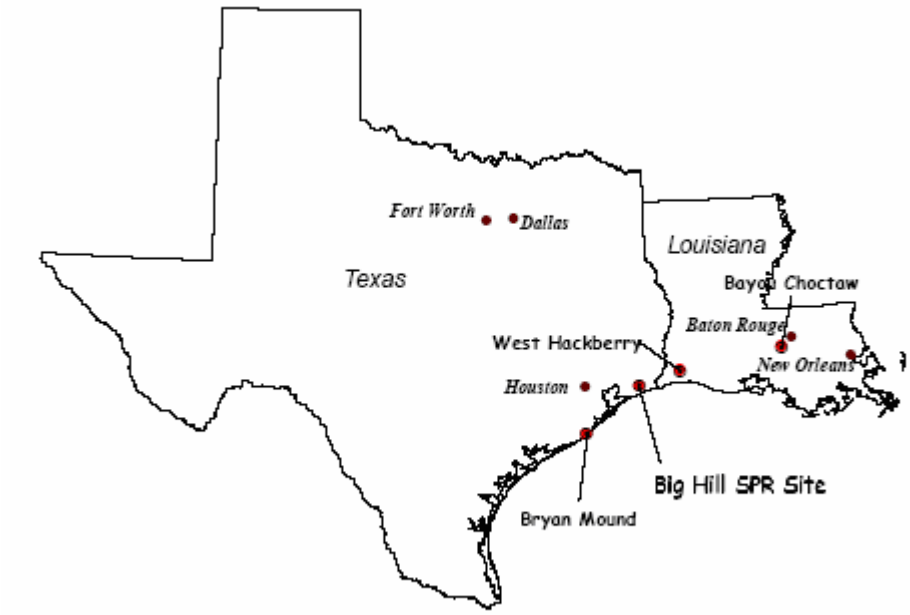

Figure 1: Location of SPR sites.

1.2 REPORT ORGANIZATION

This report is organized in the following fashion: Section 2 gives a brief description of the SPR cavern sites to show the diversity of cavern geometries in the field. Section 3 describes the analytical model, including the cavern designs, stratigraphy, material models, material properties, and damage criteria used for the analysis. Section 4 shows the results of the calculations, and identifies failure modes for the salt and the casings. Section 5 summarizes the results, and provides concluding remarks.

2. SITE DESCRIPTION

Figure 2 shows a plan view of the Big Hill site with contour lines defining the approximate location of the salt dome's edge (± 300ft) near the top (orange) and bottom (green) of the caverns. The current 14 cavern (101-114) locations and shapes are included. The figure also shows the undeveloped area north of the DOE property line (Sabine Pass Terminal) and the two smaller non-SPR caverns.

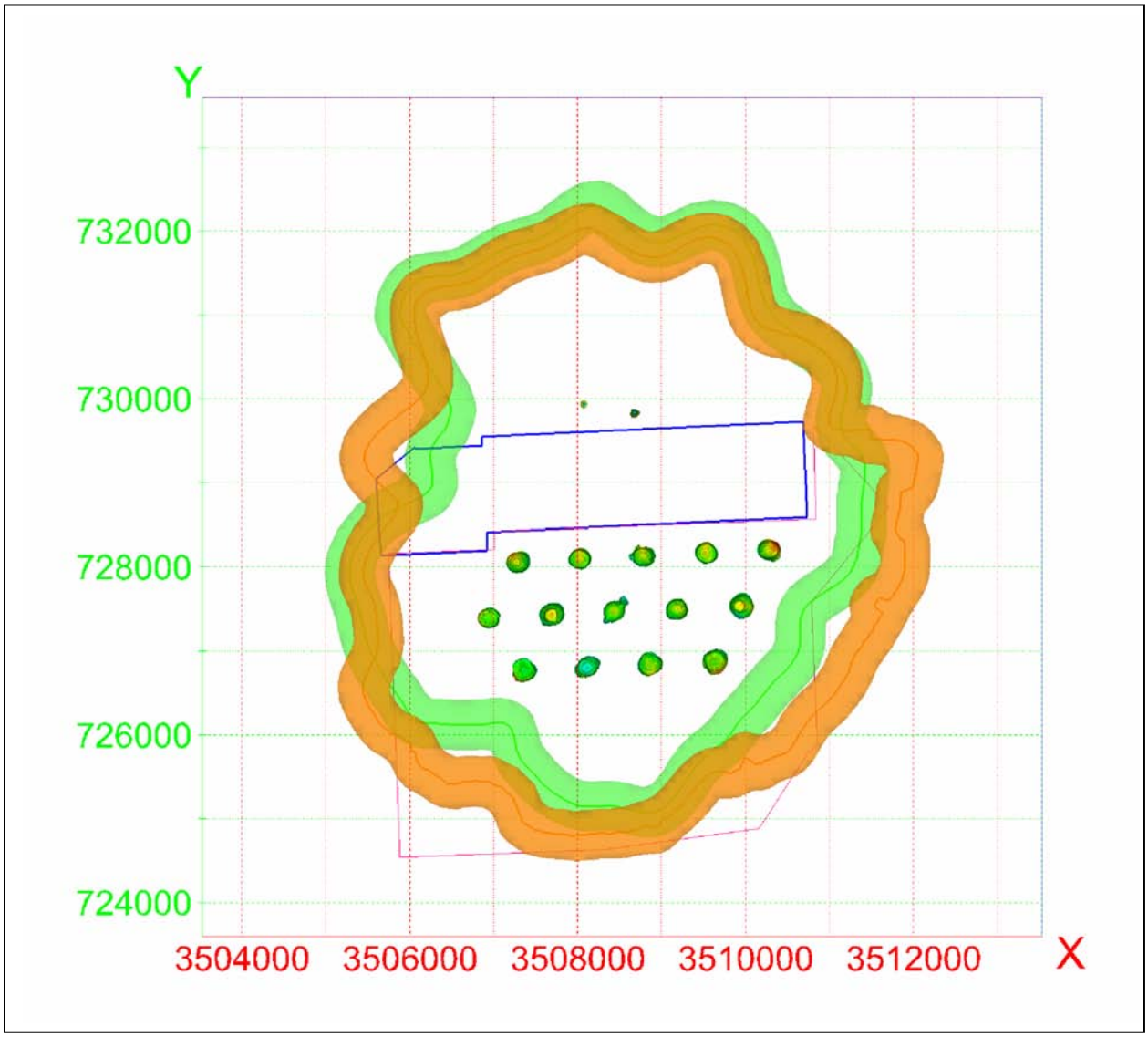

Figure 2: Site plan view of the Big Hill site (Stein, 2005b)

A geologic perspective of the salt dome and caprock are provided in Figure 3. The site has an exceptionally thick caprock comprised of two layers. The upper caprock is made of gypsum and limestone, whereas the lower caprock is made of anhydrite. Faulting also occurs in the region. A major fault extends North-South running along the entire distance of the caprock, and which extends for an unknown distance into the salt.

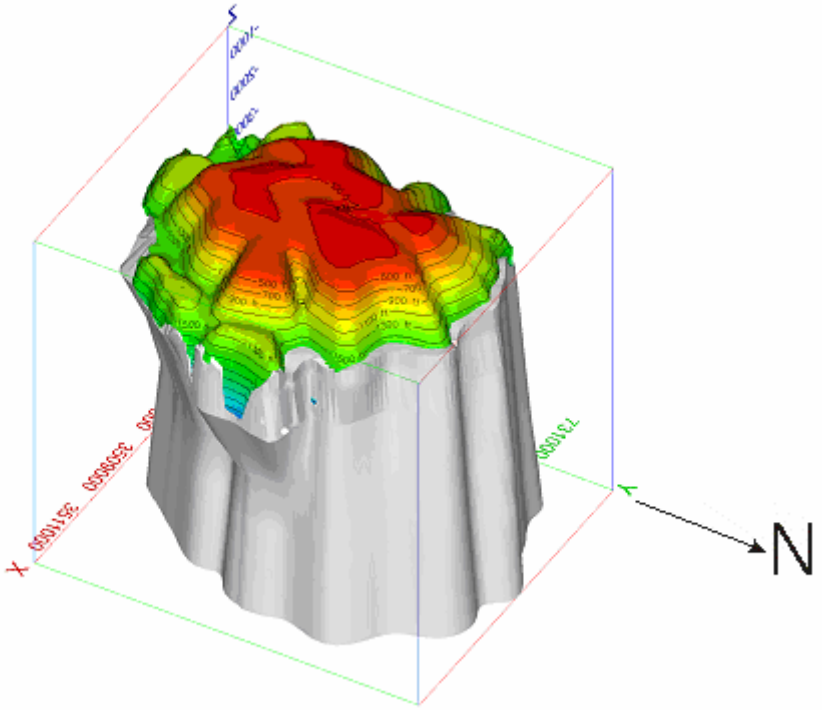

Figure 3: Perspective view of salt dome and caprock (Rautman, 2005)

Figure 4 shows the cavern geometries based on sonars at the Big Hill site. Note the enlarged tops and asymmetries of the cavern shapes. In general, caverns in the SPR are intentionally shaped with larger tops to accommodate future oil drawdowns where the bottom portions of the caverns are preferentially leached, and hence the overall cavern shape becomes more cylindrical, due to raw water injections to remove the oil. In practice, the future shapes of caverns will depend upon the drawdown and refill scenarios. As a result, caverns shapes with enlarged bottoms and mid-sections are possible (Levin, 2004). Salt properties also result in unpredictable cavern shapes as the insoluble content or dissolution rates of salt can spatially vary. This explains some of the asymmetries found in the cavern shapes. As a result, cavern shapes will vary with future drawdowns and a variety of shapes are currently found in the SPR. Some of the SPR caverns were acquired through purchase. These caverns can have unusual shapes as they were not intentionally leached for product storage, but were used to produce brine. As a result a wide variety of cavern shapes exist for the SPR and the relative advantages and disadvantages of the shapes are not clear. The analyses described in this report are designed to examine the effect on cavern stability with variations in cavern shapes and sizes. The results will be useful in evaluating current and future shapes of existing cavern, and will provide insight for designing future expansion caverns. The analyses employ a stratigraphy and material properties corresponding to the Big Hill site, but evaluate different cavern shape geometries.

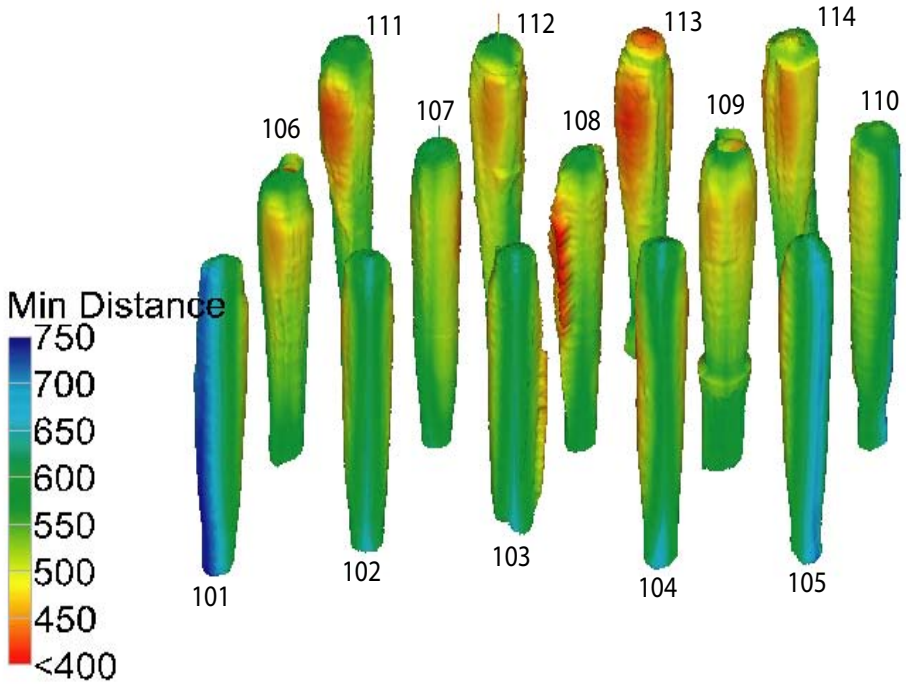

Figure 4. 3-D View from the north of recent cavern sonars showing minimum separation distances at Big Hill (Stein, 2005a)

3. ANALYSIS MODEL

3.1 MODEL DESCRIPTION

The analytical model is similar to that previously used to simulate other SPR cavern fields (Ehgartner and Sobolik, 2002). The analysis simulates caverns that were leached to full size over a one year period, filled with oil, and then permitted to creep for an additional 45 years. The standard pressure condition applied to the cavern was based on an average wellhead pressure of 945 psi. This constant pressure is applied except for planned workover periods, during which the wellhead pressure is dropped to 0 psi. These workover periods are designed to last for three months, and to occur once every 5 years. Previous analyses have shown that this abrupt pressure drop will induce the greatest potential for damage. The duration of the simulated workover may be slightly longer than is typically encountered in the field, but is chosen to provide an adverse condition and closely simulate actual subsidence measurements.

In order to perform a well stability analysis that investigates damage in salt, the analytical tools ideally need to be able to perform the following functions: 1) calculate the changes in the in situ stress field and deformations surrounding the well and cavern over a long period of time due to the creep deformation of the salt; 2) include criteria by which tensile failure or shear damage of the salt can be determined and located; 3) have the ability to reduce the time step of the analysis to discretize short-time events such as changes in cavern pressure due to workover; and 4) allow post-processing to be able to identify high strain and failure regions and compute volume changes. The computational models utilized the finite element code JAS3D (ideal for simulations of processes occurring over many years), the power law creep model for salt, and a three-dimensional, 30-degree wedge designed to model a 19-cavern field.

3.2 STRATIGRAPHY AND COMPUTATIONAL MESH

The mesh for the computational model is illustrated in Figure 5. The 19-cavern, 30-degree wedge format used for by several previous SPR calculations is applied for these calculations as well. Figure 5 refers to Caverns 1, 2, 3, and 4; Cavern 1 represents one cavern, at the center of the 19-cavern field, and Caverns 2, 3, and 4 each represent 6 caverns in the field due to model symmetry. Four material blocks are used in the model to describe the stratigraphic layers: the overburden, two layers of caprock, and the salt dome. The overburden is made of sand, the upper caprock layer is made of gypsum or limestone, and the lower caprock layer is made of anhydrite. This stratigraphic material closely matches that used for Big Hill (Park et al., 2005), and it is thought to be reasonably accurate for the other SPR sites. For simplifying the mesh, the stratigraphic layers of the cavern field are extended horizontally throughout the mesh, rather than trying to model the rocks surrounding the salt dome. The standard stratigraphy and cavern dimensions are listed in Table 1.

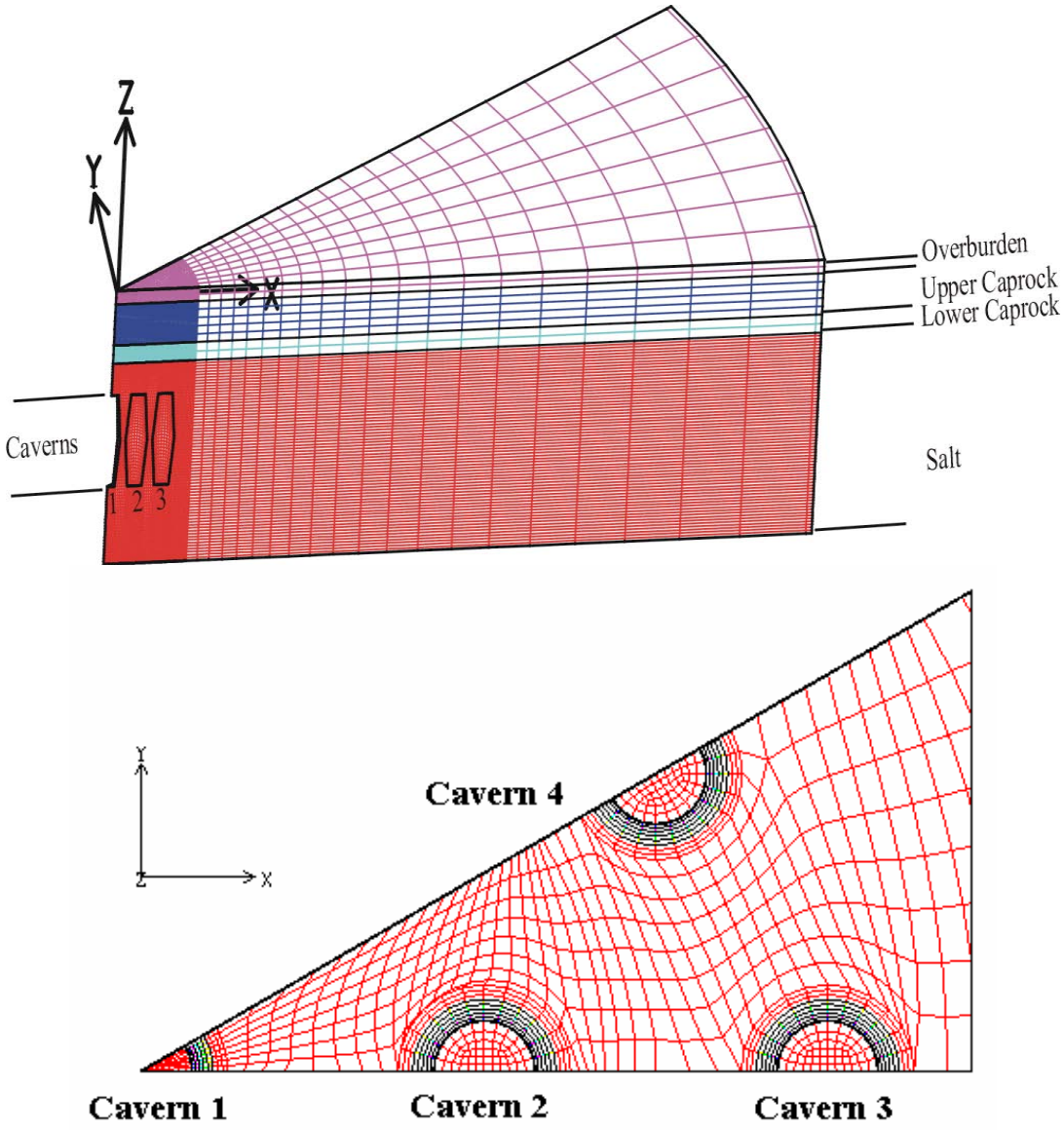

Figure 5. Finite element mesh with cross-section through caverns (plan view).

Table 1: Cavern and stratigraphy dimensions used in cavern shape analyses.

Dimension	Length
Well depth (surface to top of cavern)	2300 ft (701 m)
Initial cavern spacing, center-to-center	750 ft (228.6 m)
Initial cavern height	2000 ft (576 m)
Depth to top of salt layer	1600 ft (487.7 m): 300 ft overburden, 900 ft upper caprock 400 ft lower caprock

Four standard cavern shapes are considered in these analyses: cylindrical, enlarged top, enlarged middle, and enlarged bottom. These shapes are illustrated in detail in Figures 6 through 9. There are 17 cases in all, varying cavern shape and volume for a given base radius which is representative of current conditions based on our sonar data. Table 2 lists the 17 cases that will be considered in this analysis; caverns of different shapes for a given base radius are approximately equal in volume to the cylindrical cavern with the same base radius. Minimum and average pillar to diameter (P/D) ratios and cavern volumes (in MMB=millions of barrels) are calculated for each case. The intent is to see if there is any advantage to the use of one or the other in developing criteria to evaluate caverns.

The quantity "P/D ratio" is defined in the Level III Design Criteria for the SPR (DOE, 2001). "Pillar" refers to the minimum thickness of the web of salt remaining between any two adjacent caverns, or between the cavern and salt dome perimeter. "Diameter" refers to the average cavern diameter. To ensure cavern structural integrity, the Level III criteria mandate that the P/D ratio for each cavern must remain greater than 1.78 after five complete drawdown cycles. Typically in the field, cavern shapes are not uniformly sized, spaced, and shaped cylinders, and the definition of the Level III P/D ratio is perhaps inadequate. Stein (2005a) provides a method to develop a three-dimensional P/D ratio based on cavern measurement data. Two alternate definitions for the P/D ratio for non-constant cavern diameters are introduced in this report. The minimum P/D ratio is calculated at the point of minimum pillar thickness, i.e., minimum pillar thickness/maximum cavern diameter. The average P/D ratio is obtained by integrating the P/D at every elevation along the height of the caverns and dividing by the height. For the cases simulated in this report, the cavern diameter is a known linear function of height, and an average P/D ratio may be derived. For example, for the radius of the enlarged top (or bottom) cavern r, radius of the smaller end r_0, a 100-ft difference between smaller and larger radii, a 750-ft center-to-center cavern spacing, and normalized height of the cavern x, x={0,1}, the following expression is obtained for the average P/D:

$$
\begin{aligned}
& r = r_0 + 100x; \\
& \frac{P}{D} = \frac{(\text{center} - \text{to} - \text{center distance between caverns}) - (\text{cavern diameter})}{\text{cavern diameter}} \\
& \quad = \frac{750 - 2r}{2r} = \frac{750}{2r_0 + 200x} - 1; \qquad (1) \\
& \left(\frac{P}{D}\right)_{avg} = \frac{\int \frac{P}{D} dx}{x(=1)} = \int_0^1 \frac{750}{2r_0 + 200x} dx - \int_0^1 dx = \frac{750}{200}\left(\ln \frac{200 + 2r_0}{2r_0}\right) - 1.
\end{aligned}
$$

The Level III, minimum, and average P/D ratios for all 17 computational cases are provided in Table 2. All the cavern shape-P/D ratio cases described in Table 2 require that all caverns are the same shape (i.e., no mixing of shapes within a calculation), and initial cavern dimensions and spacing between the axes of adjacent caverns are uniform.

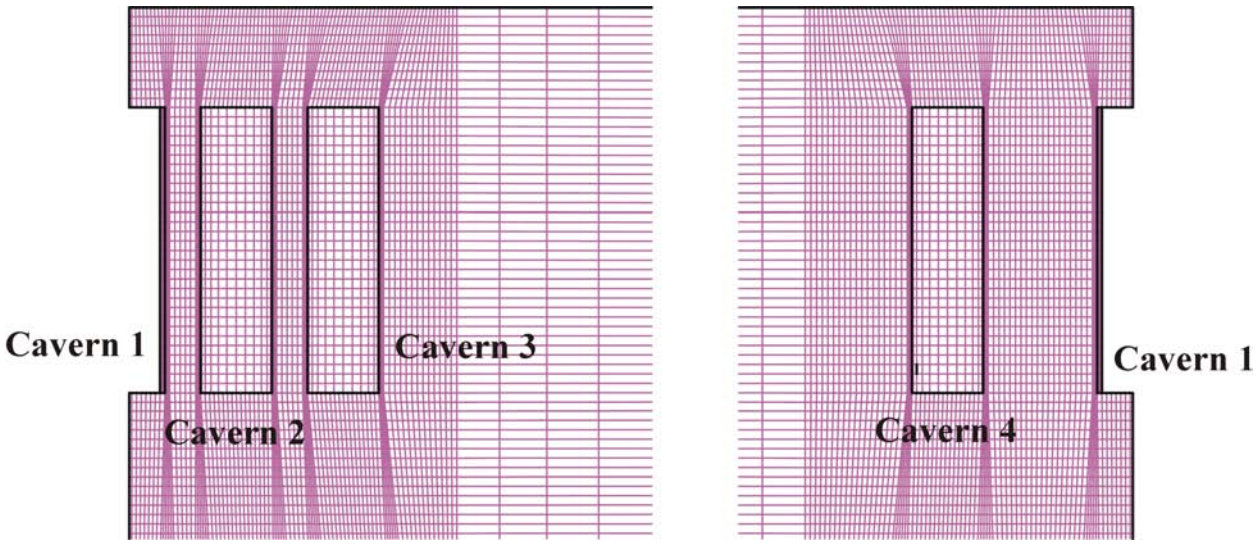

Figure 6. Mesh for cylindrical caverns, base radius 250ft.

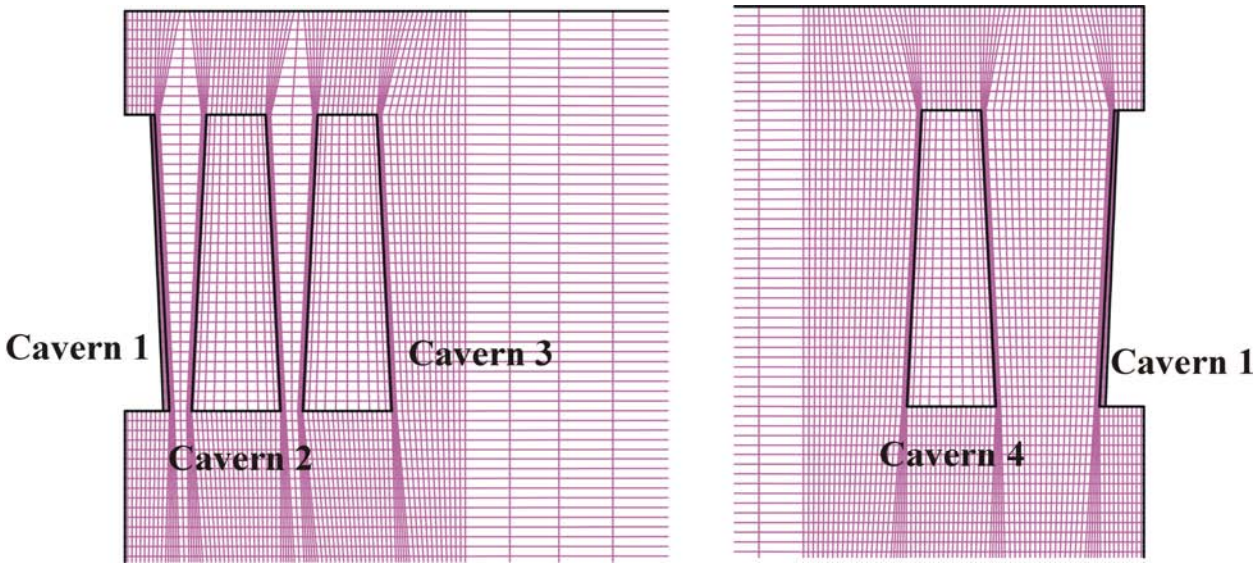

Figure 7. Mesh for enlarged bottom caverns, base radius 250ft.

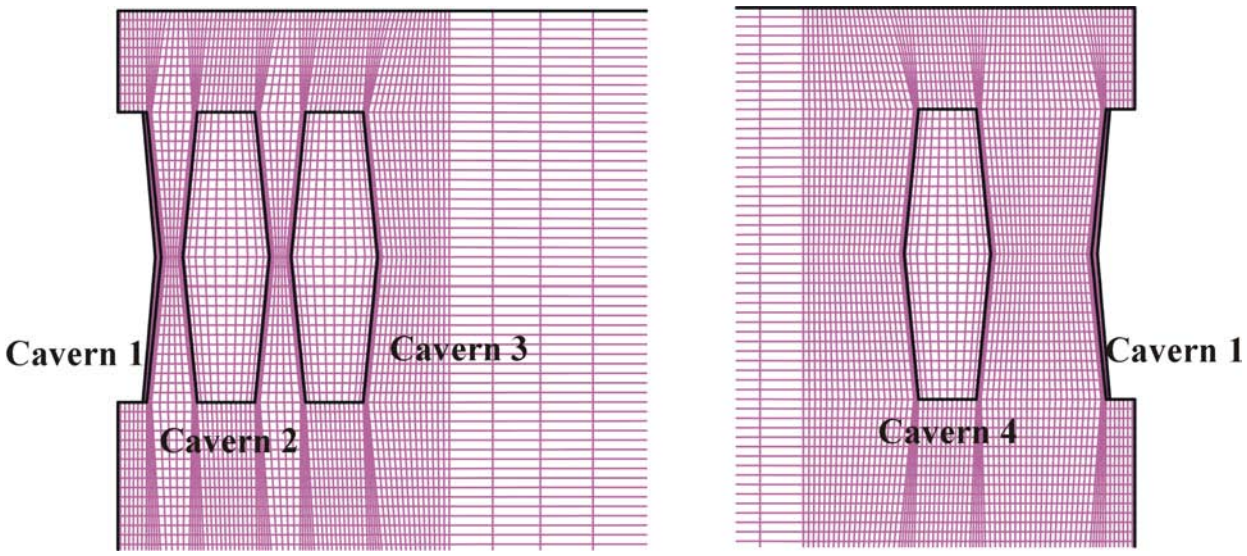

Figure 8. Mesh for enlarged middle caverns, base radius 250ft.

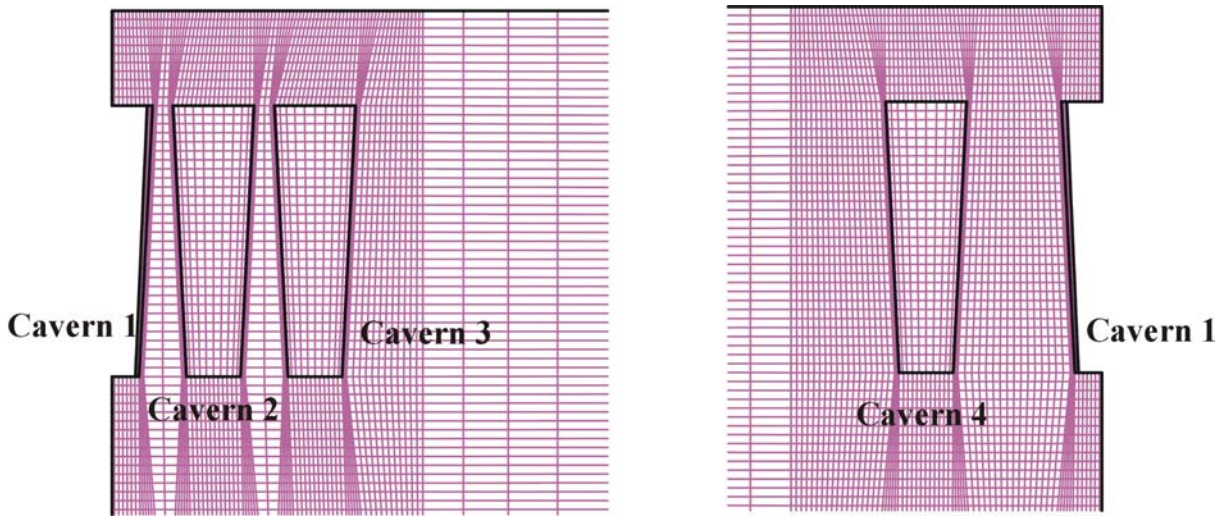

Figure 9. Mesh for enlarged top caverns, base radius 250ft.

Table 2. Cavern shape case summary.

	Radius at heights			Volume, MMB	P/D at heights			Min. P/D	Avg. P/D	Level III P/D
Base radius	0	1000	2000		0	1000	2000			
100	100	100	100	11.19	2.75	2.75	2.75	2.75	2.75	2.75
150	150	150	150	25.18	1.5	1.5	1.5	1.5	1.5	1.5
200	200	200	200	44.76	0.875	0.875	0.875	0.875	0.875	0.875
250	250	250	250	69.94	0.5	0.5	0.5	0.5	0.5	0.5
300	300	300	300	100.72	0.25	0.25	0.25	0.25	0.25	0.25
100	150	100	50	12.12	1.5	2.75	6.5	1.5	3.12	2.25
150	200	150	100	26.11	0.875	1.5	2.75	0.875	1.60	1.17
200	250	200	150	45.70	0.5	0.875	1.5	0.5	0.92	0.63
250	300	250	200	70.88	0.25	0.5	0.875	0.25	0.52	0.30
100	50	150	50	12.12	6.5	1.5	6.5	1.5	3.12	2.25
150	100	200	100	26.11	2.75	0.875	2.75	0.875	1.60	1.17
200	150	250	150	45.70	1.5	0.5	1.5	0.5	0.92	0.63
250	200	300	200	70.88	0.875	0.25	0.875	0.25	0.52	0.30
100	50	100	150	12.12	6.5	2.75	1.5	1.5	3.12	2.25
150	100	150	200	26.11	2.75	1.5	0.875	0.875	1.60	1.17
200	150	200	250	45.70	1.5	0.875	0.5	0.5	0.92	0.63
250	200	250	300	70.88	0.875	0.5	0.25	0.25	0.52	0.30

To simulate actual field workover conditions, not all caverns are in workover mode at the same time. The central cavern in the field is the first cavern in the workover sequence beginning one year after initial cavern leaching. It is worked over every 5 years until the end of the simulations. The next closest neighboring cavern is due to be worked over the following year (Number 2 in Figure 5). Because of mesh symmetry, workover pressures must be applied to the entire second (inner) ring of caverns at the same time. This results in the 6 neighboring caverns at low pressure starting one year after each workover of the central cavern. The workover sequence continues with the outer ring of caverns (Cavern 3 in Figure 5) being subject to workover pressures one year after the inner ring, followed by the intermediate ring of caverns (on the 30° symmetry plane, Well 4 in Figure 5) in workover mode a year later. The convention used to discuss these rings of caverns in the model is to simply refer to them as caverns 1 (central cavern), 2 (the inner set of six caverns) 3 (outer set of six caverns along the 0°symmetry plane), and 4 (intermediate ring located along the 30° symmetry plane).

3.3 NUMERICAL AND MATERIAL MODELS

This analysis utilized JAS3D, Version 2.0.F (Blanford et al., 2001); a three-dimensional finite element program developed by Sandia National Laboratories, and designed to solve large quasi-static nonlinear mechanics problems. Several constitutive material models are incorporated into the program, including models that account for elasticity, viscoelasticity, several types of hardening plasticity, strain rate dependent behavior, damage, internal state variables, deviatoric creep, and incompressibility. The continuum mechanics modeled by JAS3D are based on two fundamental governing equations. The kinematics are based on the conservation of momentum equation, which can be solved either for quasi-static or dynamic conditions (a quasi-static procedure was used for these analyses). The stress-strain relationships are posed in terms of the conventional Cauchy stress.

The power law creep model has been used for Waste Isolation Pilot Plan (WIPP) and Strategic Petroleum Reserve (SPR) simulations for many years. Values for the creep constant, the stress exponent, and the thermal activation energy constant for the power law creep model have been obtained for hard and soft salts through mechanical property testing of salt cores collected from boreholes (Wawersik and Zeuch, 1984; Munson, 1998). These properties have been further modified by matching site subsidence and cavern volume loss data (Ehgartner and Sobolik, 2002; Park et al., 2005). The creep constitutive model considered only secondary or steady-state creep. The creep steady state strain rate is determined from the effective stress as follows:

$$\dot{\varepsilon} = A_2\left(\frac{\sigma}{\mu}\right)^n \exp\left(-\frac{Q}{RT}\right) = A(\sigma)^n \exp\left(-\frac{Q}{RT}\right), \quad A = \frac{A_2}{\mu^n} \tag{2}$$

where, $\dot{\varepsilon}$ = creep strain rate,

σ = effective or von Mises stress,

μ = shear modulus, E/2(1+ν),

T = absolute temperature,

A_2, A, n = constants determined from fitting the model to creep data,

Q = effective activation energy,

R = universal gas constant.

The properties assume a homogeneous material, and are generally obtained from laboratory measurements. In order to obtain agreement with the measured closure of underground drifts at the WIPP, a reduced modulus is used to simulate the transient response of salt (Morgan and Krieg, 1990). The elastic modulus reduction factor (RF) is known to vary for salts (Munson, 1998). Limited creep testing of SPR salts (Wawersik and Zeuch, 1984) showed considerable variability in creep rates (up to an order of magnitude difference). For the West Hackberry and Big Hill sites, a value for RF of 12.5 was determined by calibrating to best match the measured closure and subsidence rates at those sites through back-fitting analysis. For these analyses, the same reduction factor will be used for the moduli.

3.4 MATERIAL PROPERTIES

The Big Hill and West Hackberry salts are identified in Munson (1998) as "soft" salts, as opposed to "hard" salts at Bayou Choctaw and Bryan Mound. These analyses were designed to consider the greater potential for deformation of the soft salts. The salt properties used for these analyses are based on properties published by Park et al. (2005) derived for the Big Hill site. These properties are listed in Table 3. The modulus values in Table 3 are obtained from the standard modulus values in Munson (1998) divided by a reduction factor of 12.5.

Table 3. Power Law Creep Mechanical Properties Used for Salt

Property	Big Hill Properties (Park et al., 2005)
Density, kg/m^3	2300
Elastic modulus, GPa	2.48
Bulk modulus, GPa	1.65
Shear modulus, GPa	0.992
Poisson's ratio	0.25
Creep Constant A, 1/(Pa^n-sec)	8.69×10^{-36}
Exponent n	4.9
Thermal constant Q/R, K	6034

The anhydrite as simulated in the lower caprock layer is expected to experience inelastic material behavior. The anhydrite layer is considered isotropic and elastic until yield occurs (Butcher, 1997). The behavior of the anhydrite is assumed to be the same as the WIPP anhydrite. Once the yield stress is reached, plastic strain begins to accumulate. Yield is assumed to be governed by the Drucker-Prager criterion.

$$\sqrt{J_2} = C - aI_1 \tag{3}$$

Where $J_2 =$ the second deviatoric stress invariant

$I_1 =$ the first stress invariant

A non-associative flow rule is used to determine the plastic strain components. Drucker-Prager constants, *C* and *a*, for the anhydrite are given in Table 4.

Table 4: Drucker-Prager constants for anhydrite (Butcher, 1997).

Parameters	Units	Values
C	MPa	1.35
a		0.45

The input to the soil and crushable foam model in the JAS3D code requires the analyst to provide the shear modulus times two, 2μ, and the bulk modulus, *K*. The conversions from Young's modulus, *E*, and Poisson's ratio, ν, to the JAS3D input parameters are given by the following relationships:

$$2\mu = \frac{E}{(1+\nu)} \tag{4}$$

$$K = \frac{E}{3(1-2\nu)} \tag{5}$$

The JAS3D code requires the input to the material model which describes the anhydrite's nonlinear response to be given in terms of effective stress, $\bar{\sigma} = \sqrt{3J_2}$, and pressure, $p = \frac{I_1}{3}$. Rewriting Equation 3 in terms of $\bar{\sigma}$ and p, the following relationship is obtained:

$$\bar{\sigma} = \sqrt{3}C - 3\sqrt{3}ap \tag{6}$$

The JAS3D input parameters A_0 and A_1 are $\sqrt{3}C$ and $3\sqrt{3}a$, respectively. A third input parameter, A_2, is used in the soil and crushable foam model to add a quadratic component (A_2p^2) to the yield function in Equation 6; the Drucker-Prager formulation in Equation 3 sets A_2=0. The JAS3D input parameters for the anhydrite are given in Table 5.

Table 5: Material properties of lower caprock (anhydrite) (Butcher, 1997).

Parameters		Units	Values
Density (ρ)		kg/m^3	2300
Young's Modulus (E)		GPa	75.1
Poisson's Ratio (ν)		-	0.35
Bulk Modulus (K)		GPa	83.4
Shear Modulus (μ)		GPa	27.8
Constants	A0	MPa	2338
	A1	-	2.338
	A2	-	0

The surface overburden layer, which is mostly comprised of sand and sandstone, is considered isotropic and elastic, and has no assumed failure criteria. The upper caprock layer, consisting of gypsum and limestone, is also assumed to be elastic. Its properties are assumed to be the same as those used for the West Hackberry analyses (Ehgartner and Sobolik, 2002). Mechanical properties of each of these geologic materials used in the present analysis are listed in Table 6.

Table 6: Material properties of overburden and upper caprock layers.

Parameters	Units	Overburden	Upper caprock
Density	kg/m^3	1874	2500
Young's Modulus	GPa	0.1	7.0
Poisson's Ratio		0.33	0.29

3.4 DAMAGE CRITERIA

Four measures of cavern performance are evaluated in this study. The first uses safety factors as identified by two separate dilatant damage criteria: one a linear function of the hydrostatic pressure (Van Sambeek et al., 1993), and the other based on laboratory data from samples of Big Hill salt (Lee et al., 2004). Dilatancy is considered the onset of damage to rock resulting in significant increases in permeability. Dilatant damage in salt typically occurs at the point at which a rock reaches its minimum volume, or dilation limit, at which point microfracturing in the rock increases the volume. Dilatant criteria typically relate two stress invariants: the mean stress invariant I_1 (equal to three times the average normal stress) and the square root of the stress deviator invariant J_2, or $\sqrt{J_2}$ (a measure of the overall deviatoric or dilatant shear stress). One dilatant criterion is the equation typically used from Van Sambeek et al. (1993), $\sqrt{J_2} = 0.27 I_1$. This damage criterion defines a linear relationship between I_1 and $\sqrt{J_2}$, and such a linear relationships have been established from many suites of lab tests on WIPP, SPR, and other salt samples. The other dilatant criterion is based on laboratory tests performed on samples of salt from the Big Hill site, which is categorized as a soft salt. The criterion is a curve fit to data taken from triaxial compression tests performed at several values of confining pressure (Lee et al., 2004). The equation for this criterion is given as:

$$\sqrt{J_2}(MPa) = 12.04 - 9.104 e^{-0.04931 I_1(MPa)} \tag{7}$$

These criteria were applied during post-processing of the analyses. Safety factor indices were created for each criterion (SF_{VS}, SF_L) by normalizing I_1 by the given criterion:

$$SF_{VS} = \frac{0.27 I_1}{\sqrt{J_2}}; \quad SF_L = \frac{12.04 - 9.104 e^{-0.04931 I_1(MPa)}}{\sqrt{J_2}} \tag{8}$$

Several earlier publications define that the Van Sambeek safety factor SF_{VS} indicates damage when $SF_{VS}<1$, and failure when $SF_{VS}<0.6$. The Lee safety factor indicates dilatant damage when $SF_L<1$. This report will use these damage thresholds.

A comparison of the two dilation criteria is shown in Figure 10. The Van Sambeek criterion is representative of a large data base of salts and is therefore considered typical of salt. Big Hill salt was found to have a unique criterion. The Van Sambeek criterion is more conservative for mean normal stress values of about 1700 psi (11.7 MPa); above this stress, the Lee damage criterion becomes much more conservative. Because the Van Sambeek index has a longer history based on many more laboratory tests, it is of greater interest than the Lee index developed for Big Hill salt; although both indices are used here to evaluate the impact of cavern shape on damage zones, the Van Sambeek index will be emphasized.

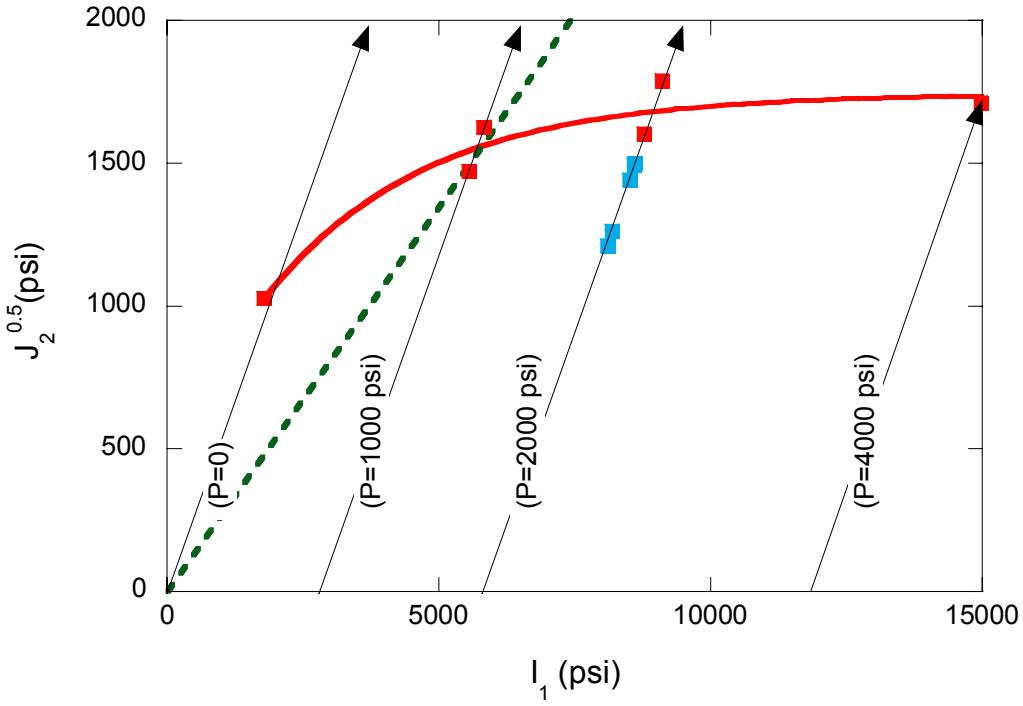

Figure 10. Dilation criterion (red line) and data of Big Hill salt compared to typical salt (green line) from Lee et al., 2004 (blue data points from Ehgartner et al. 2002).

The second cavern performance measure looks at cavern volume closure for each characteristic cavern shape. The third measure evaluates the axial well strain in the caprock above the cavern, and the fourth measure looks at the maximum subsidence at the surface for each cavern design. These measures are compared to both minimum and average P/D ratios, as well as cavern volumes, for different cavern radii.

4. RESULTS

There are many performance measures used by storage cavern designers to evaluate a cavern field. Depending on the function of the storage site, the local geological and geographical features, and the economics risks being undertaken, certain design factors of the site may take precedence over others. For example, subsidence may be a more important factor for cavern fields located near sea level, if the predicted safety factors for each shape under consideration are acceptable. At some sites, well failures in the caprock are problematic and well strains may become the dominant factor. The importance of cavern shapes will be examined by the use of four separate design factors: safety factors based on the hydrostatic pressure and deviatoric stress, cavern volume closure, axial well strain in the caprock, and surface subsidence. The cavern shapes will be ranked on the basis of each design factor, and an overall evaluation will be discussed in the conclusions section.

4.1 SAFETY FACTORS IN SALT SURROUNDING THE CAVERNS

The Van Sambeek safety factor SF_{VS} defined in Equation 8 relates the first invariant of the stress I_1 to the deviatoric stress represented by $\sqrt{J_2}$ in a linear relationship. The minimum safety factors typically occur during the workover periods, when the pressure at the wellhead is reduced to 0 psi. When the minimum safety factor in the salt is plotted as a function of time, observations can be made regarding the change in safety factor as the initial cavern radius is increased, and also as a function of time. Figures 11-14 present the minimum safety factor in salt for changing cavern radius for the four cavern types – cylindrical, enlarged bottom, enlarged middle, and enlarged top, respectively. The four cases for which the base radius was 250 feet were run out to 100 years to determine if there were any continuing trends not observed in the first 45 years. The cylindrical caverns in Figure 11 show decreasing safety factors, both at operating and at workover pressures, as the radius increases. The operating safety factors are the larger numbers on the figures, and the workover safety factors are the lowest values. For all the cylindrical cases, the operating safety factor decreases over time as the caverns close. However, for all but the 300-ft radius case, the workover safety factors remain level over time; for the 300-ft radius case, after some early factors less than 1, indicating dilatant damage, the workover safety factors increase slightly. The results are similar in Figures 13 and 14 for the enlarged middle and enlarged top caverns. In Figure 12, the enlarged bottom caverns show a different behavior, as the workover safety factors also decrease over time. This is especially noticeable in the time period after 45 years. For all these calculations, no safety factor was calculated to be in the failure range (<0.6), and only the 300-ft radius cylindrical cavern had any safety factors in the damage range (<1) during the first 45 years of operation.

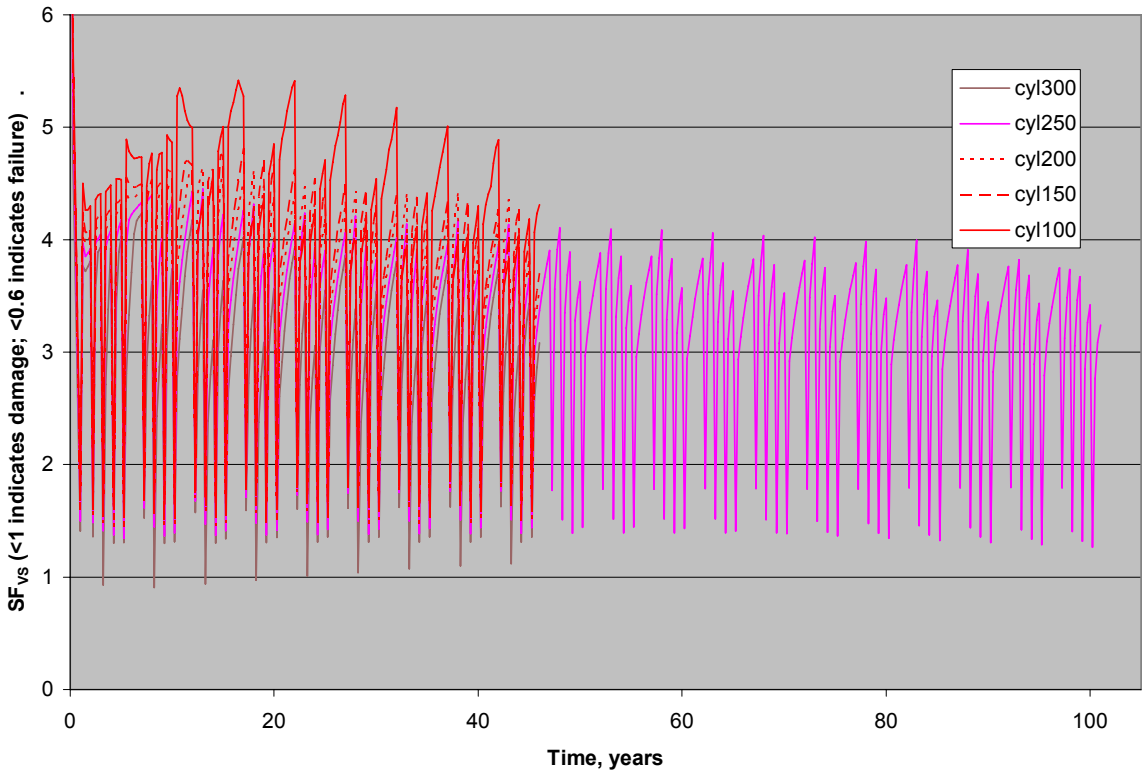

Figure 11. Minimum Van Sambeek safety factor, cylindrical caverns.

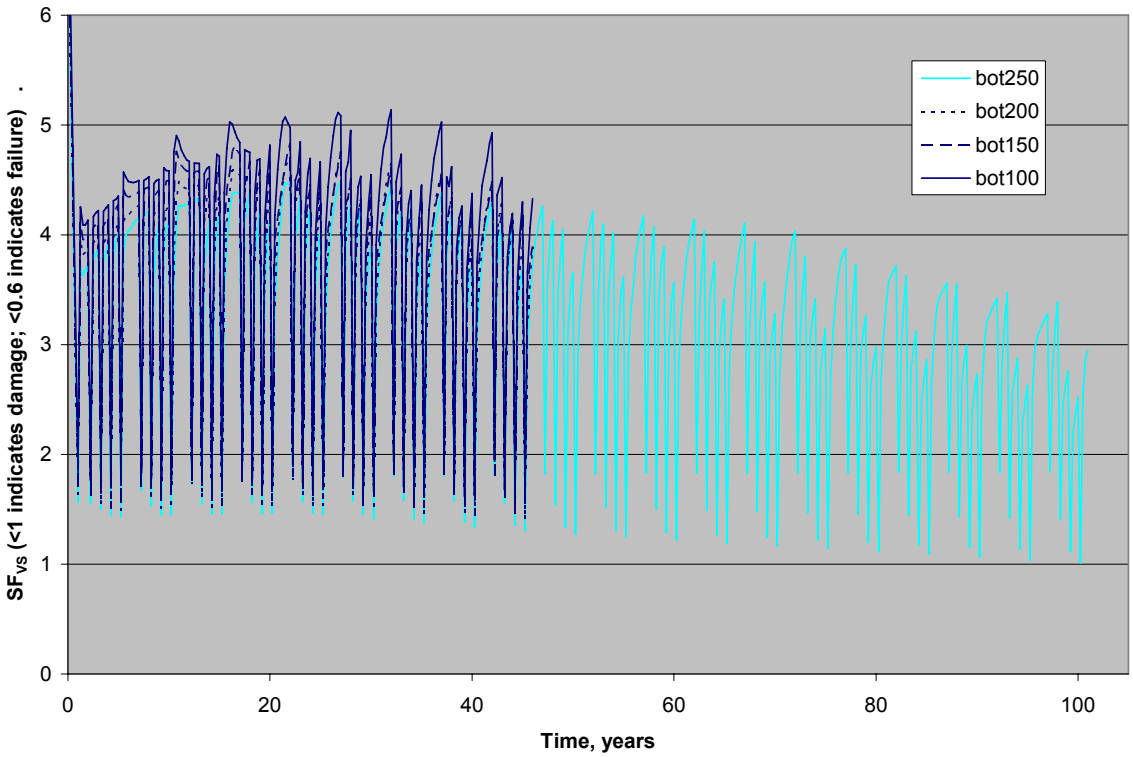

Figure 12. Minimum Van Sambeek safety factor, enlarged bottom caverns.

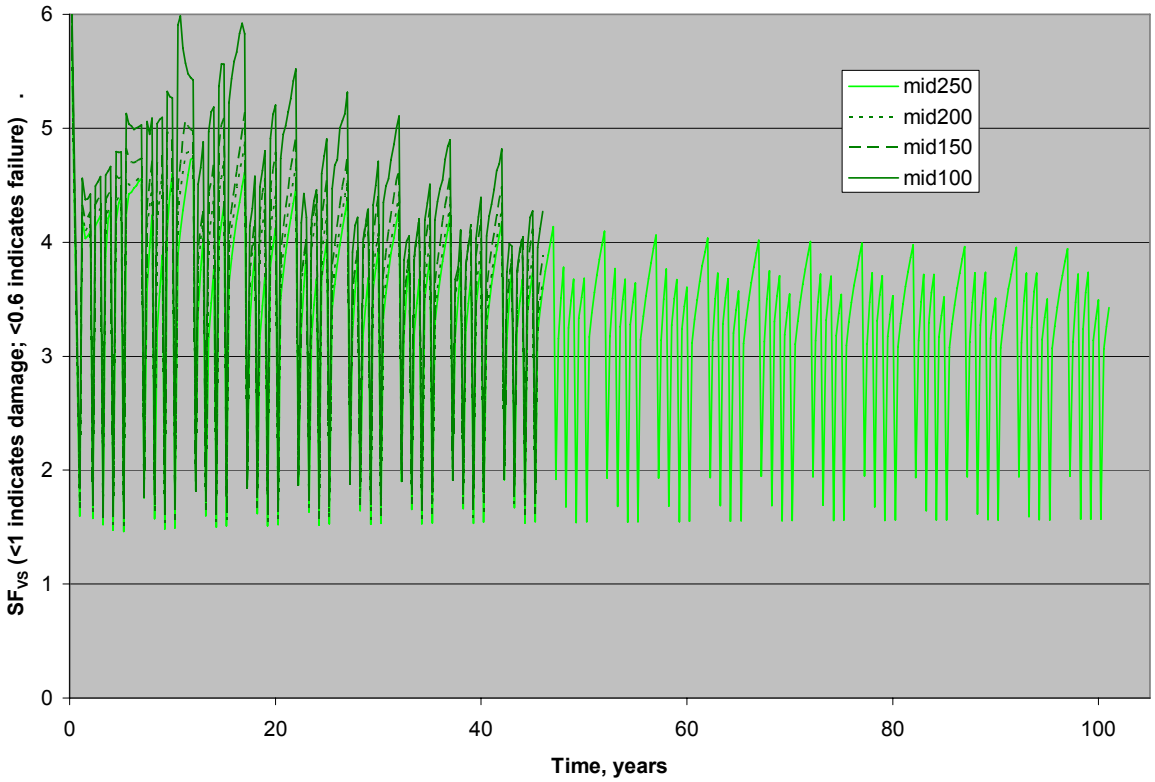

Figure 13. Minimum Van Sambeek safety factor, enlarged middle caverns.

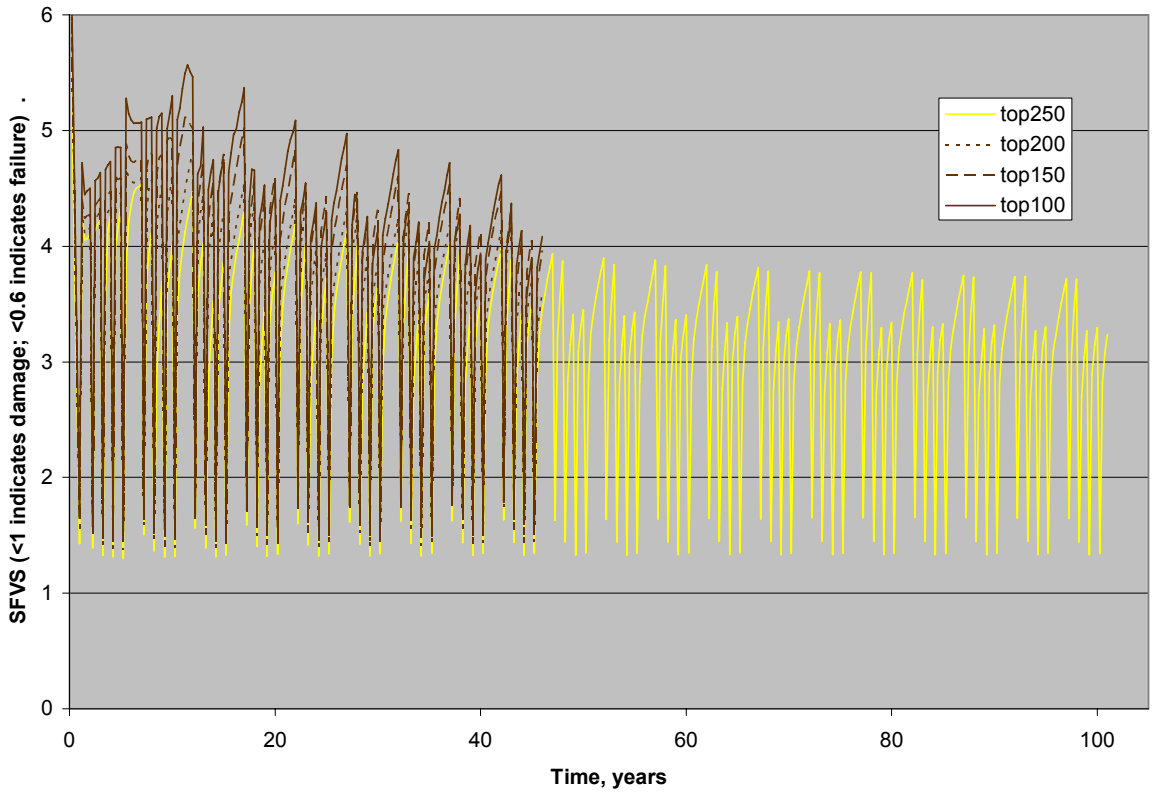

Figure 14. Minimum Van Sambeek safety factor, enlarged top caverns.

Figures 11-14 indicate that the enlarged middle caverns have the highest overall safety factors. To further investigate this trend, the minimum safety factor for each shape can be plotted as a function of an indicator of size. Figure 15 plots the minimum safety factor as a function initial cavern volume after 45 years of operation. The enlarged middle caverns clearly have the highest safety factor regardless of volume. The significant drop in safety factor for the cylindrical caverns occurs for the 300-ft base radius case. Figures 16 and 17 plot the minimum safety factor as a function of minimum and average P/D ratios, respectively. For the lowest minimum P/D in Figure 16, which corresponds to the 250-ft base radius cases for the non-cylindrical caverns and the 300-ft radius cylindrical caverns, the non-cylindrical caverns maintain a significantly higher safety factor. For comparison, Figure 17 shows similar behavior for each of the cavern shapes at similar average P/D ratios. It would seem that Figure 17 represents the fairer comparison of cavern shape effects, with the 300-ft cylindrical cavern a unique situation of having the smallest effective P/D. Based on this comparison, the average P/D ratio for a series of caverns may be a more important parameter than the minimum P/D ratio. The results shown in Figures 15 and 17 are similar enough that there may exist either a critical threshold volume or a critical threshold average P/D value for which the safety factor precipitously changes, and these thresholds may be related. Although there is some discrepancy in Figures 15-17, it appears the enlarged top caverns tend to have the lowest safety factors of the four designs. A rank order, from best performance to worst, based on safety factors would be: 1) enlarged middle; 2) enlarged bottom; 3) cylinder; and 4) enlarged top.

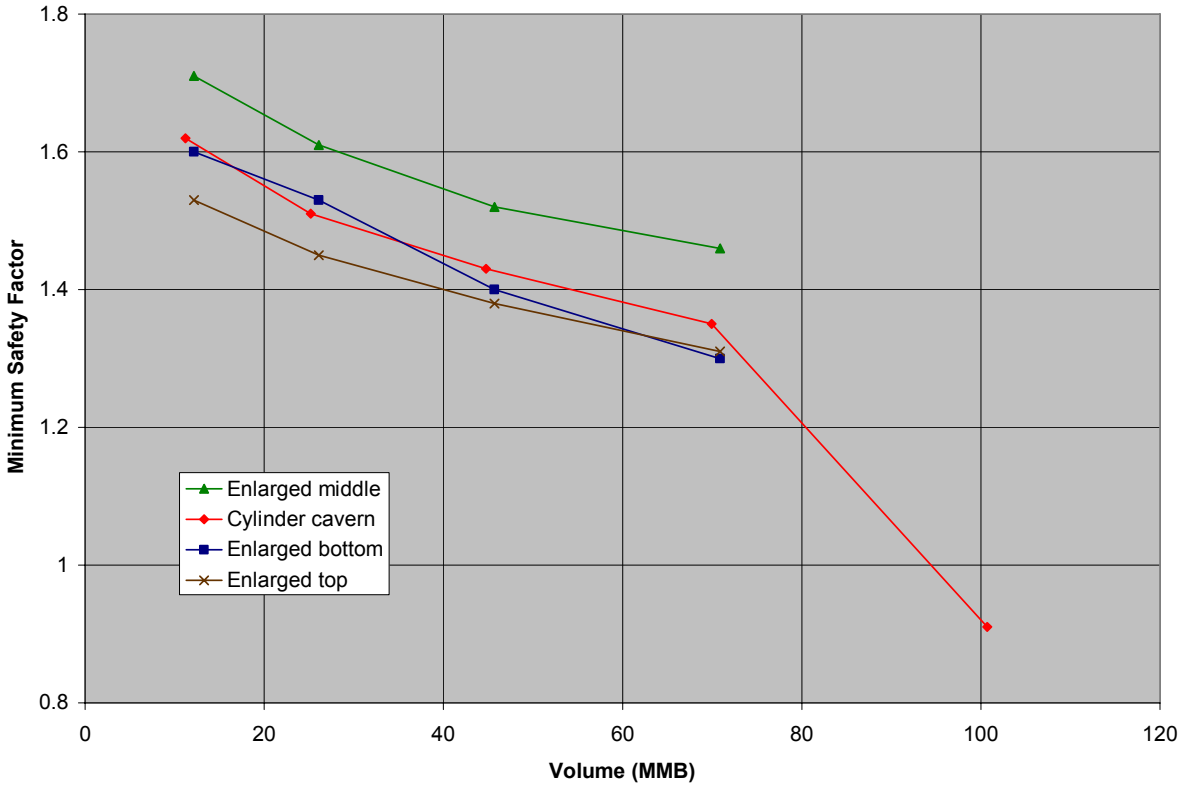

Figure 15. Minimum Van Sambeek safety factor as a function of initial cavern volume.

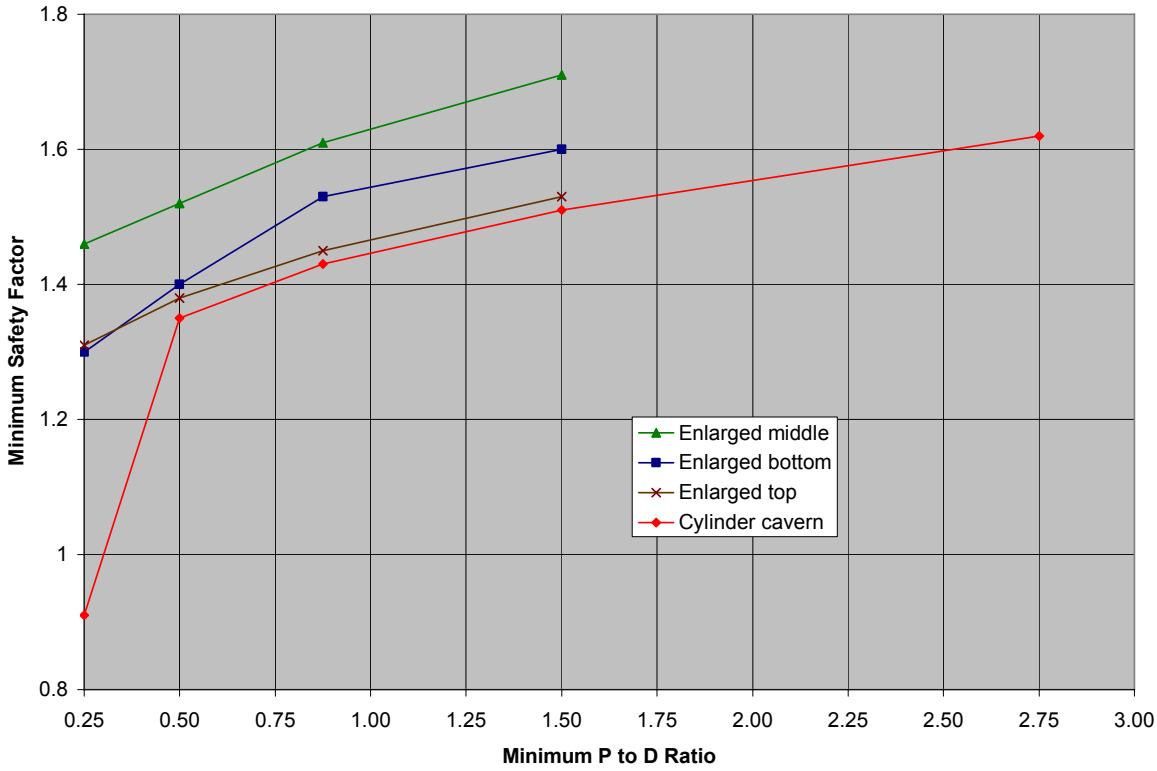

Figure 16. Minimum Van Sambeek safety factor as a function of minimum P/D ratio.

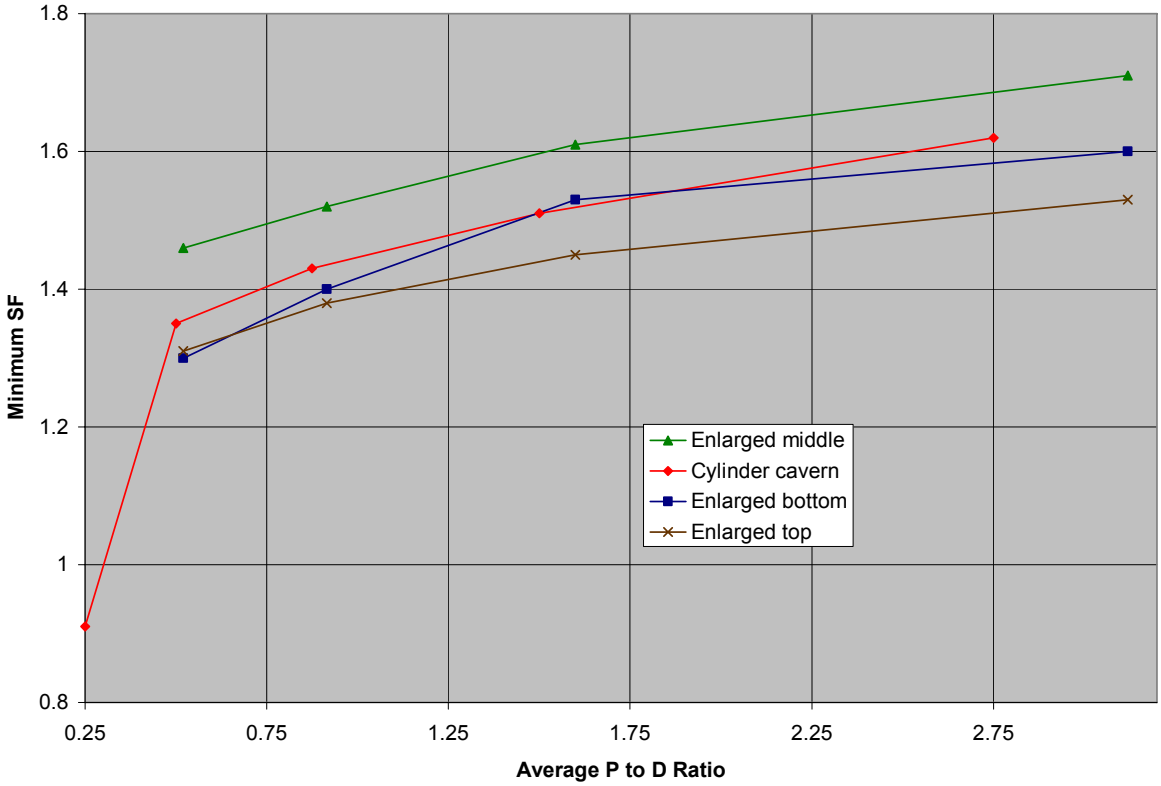

Figure 17. Minimum Van Sambeek safety factor as a function of average P/D ratio.

An additional piece of important information from these calculations is the location of the minimum safety factor, which occurs during the workover cycles. In general there is more concern associated with cavern instability when it occurs at the roof of a cavern. The potential exists for cavern collapse or partial failure resulting in rock falls that can damage the hanging strings in the cavern. However, damage in the pillar of salt separating caverns or the salt between a cavern and the edge of the dome is important regardless of location as the cavern can lose its integrity or ability to contain its product if the damage extends through the salt web.

Figure 18 shows that for all but the enlarged bottom cavern analyses (see Table 2 for explanation of cases), the location of the minimum safety factor is at the top of the cavern, either on the ceiling or on the wall very near the top. (In Figure 18, the number "10" on the vertical axis corresponds to the bottom of the cavern, "30" to the middle, and "50" to the top.) For the enlarged bottom caverns, the minimum safety factor alternates between the top and the bottom of the cavern. If an alternate safety factor based on Lee's laboratory tests on Big Hill salt is used, a different picture of the location of minimum safety factor (i.e., maximum damage) emerges. Figure 19 shows contour plots of the Lee safety factor for the enlarged top caverns at four times after 40 years – operating pressure, and workover pressures in caverns 1, 2, and 3. The location of the minimum safety factor is indicated by the crosshairs symbol. Note how the location of the minimum safety factor moves from the bottom of cavern 1 during its workover, in the top portion of cavern 2 during its workover, and at the top of cavern 3 during its workover. Figure 20 shows similar behavior for the enlarged middle caverns, with the location of minimum safety factor moving from bottom to middle and back to bottom. Figures 21 through 23 are analogous to Figure 18 in showing the history of the location of the minimum Lee safety factor for the enlarged bottom, middle, and top caverns respectively. The minimum safety factor tends to stay near the bottom of the cavern for the enlarged bottom case, although will move higher with increasing radius. It tends to stay near the middle (i.e., at the minimum P/D location) for the enlarged middle caverns, and will move around the height of the caverns for the enlarged top case, though ten to be closer to the top. Because of the near constant value of damage threshold of the deviatoric stress measure $\sqrt{J_2}$ as expressed in the Lee criterion beyond a relatively small I_1 (Figure 10), the minimum Lee safety factor indicates the location of maximum deviatoric stress. The deviatoric stress represents a large shear stress (or equivalently, a large difference between minimum and maximum stresses). Therefore, the location of the minimum Lee factor indicates regions of concerns for shear damage of the salt.

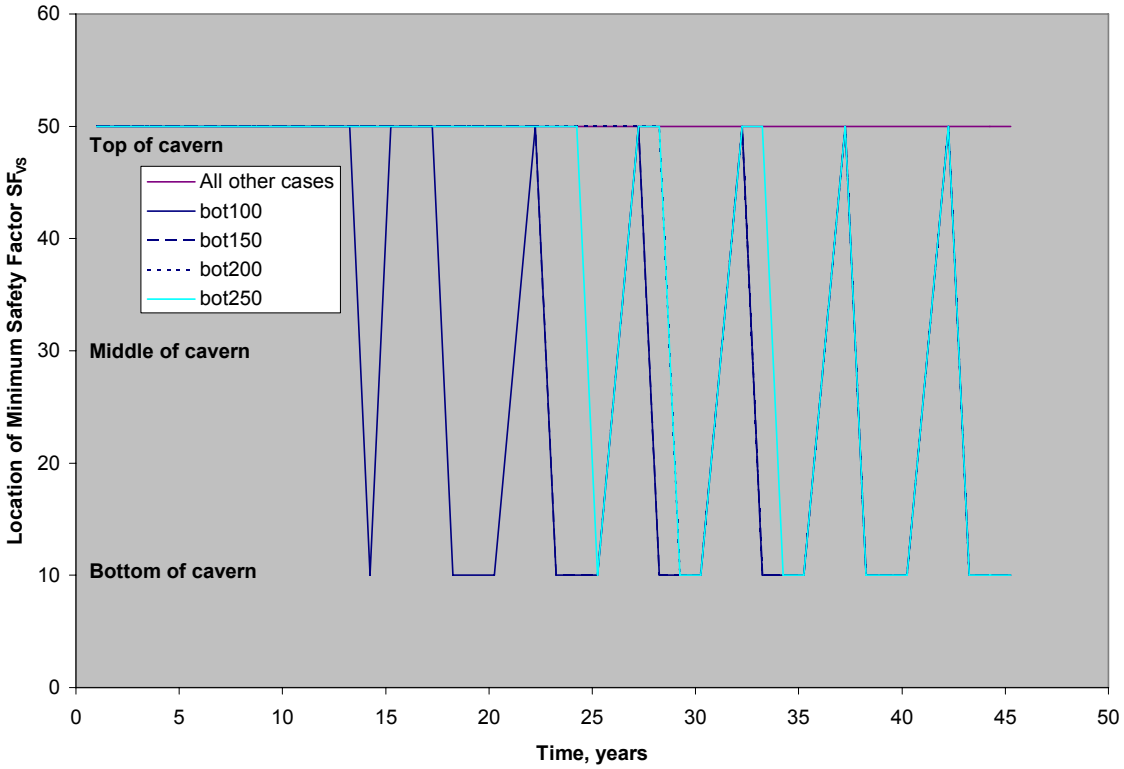

Figure 18. Location of minimum Van Sambeek safety factor during workover cycles.

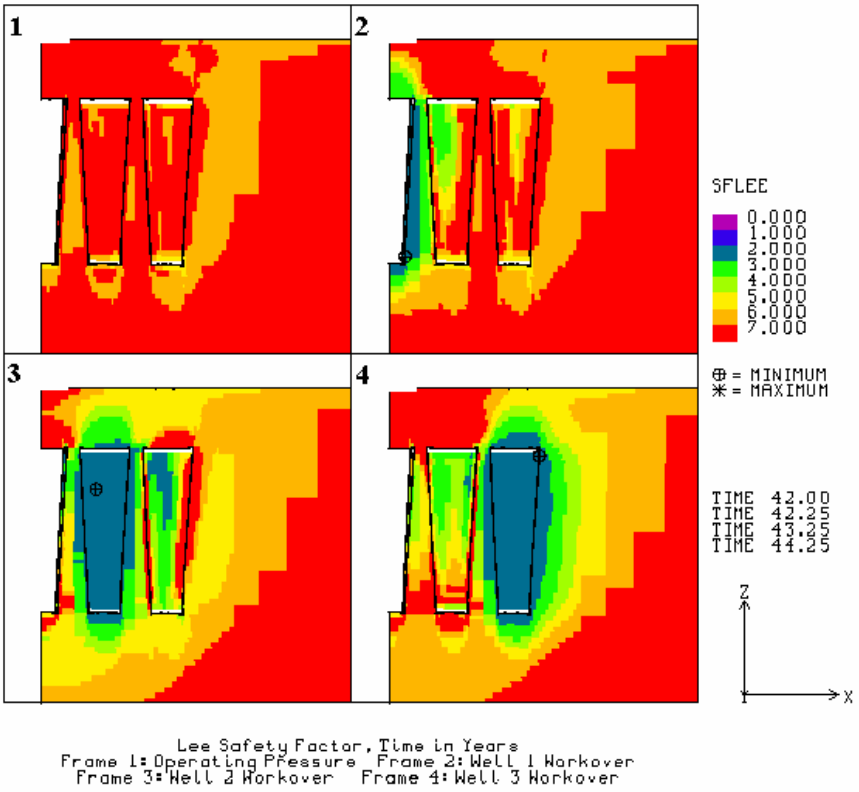

Figure 19. Contour plot of Lee safety factor, enlarged top caverns.

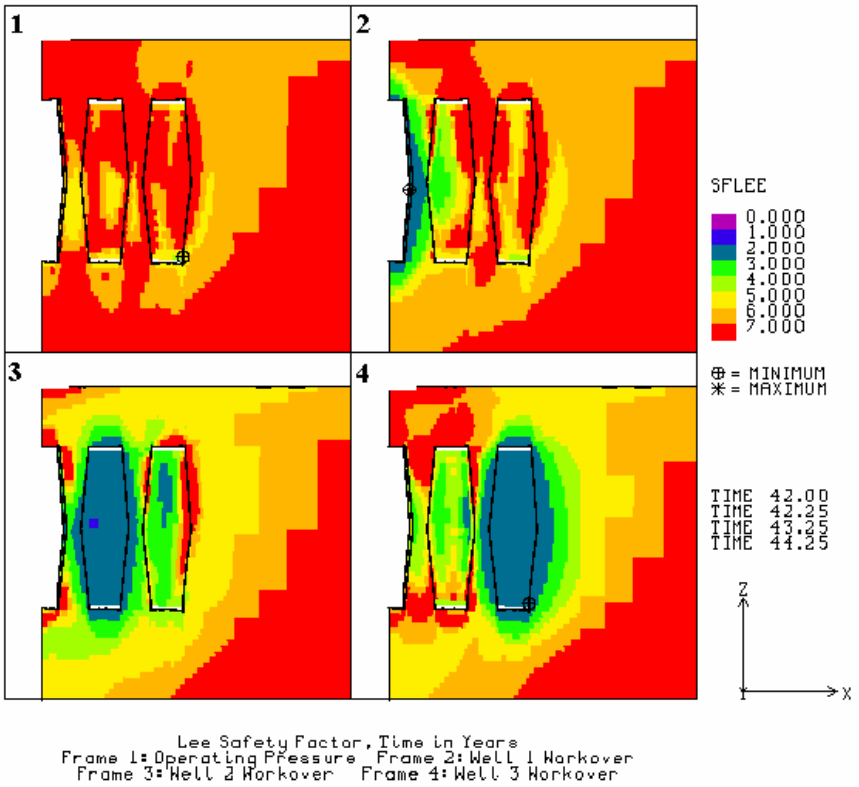

Figure 20. Contour plot of Lee safety factor, enlarged middle caverns.

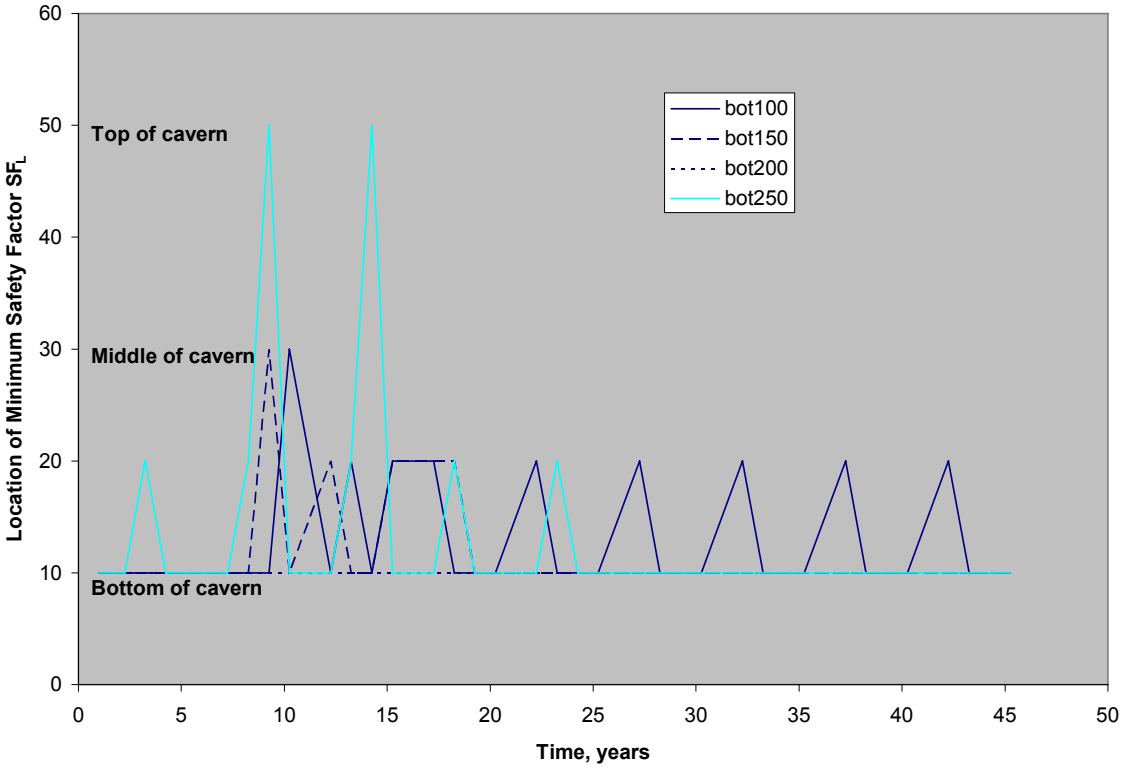

Figure 21. Location of minimum Lee safety factor, enlarged bottom caverns.

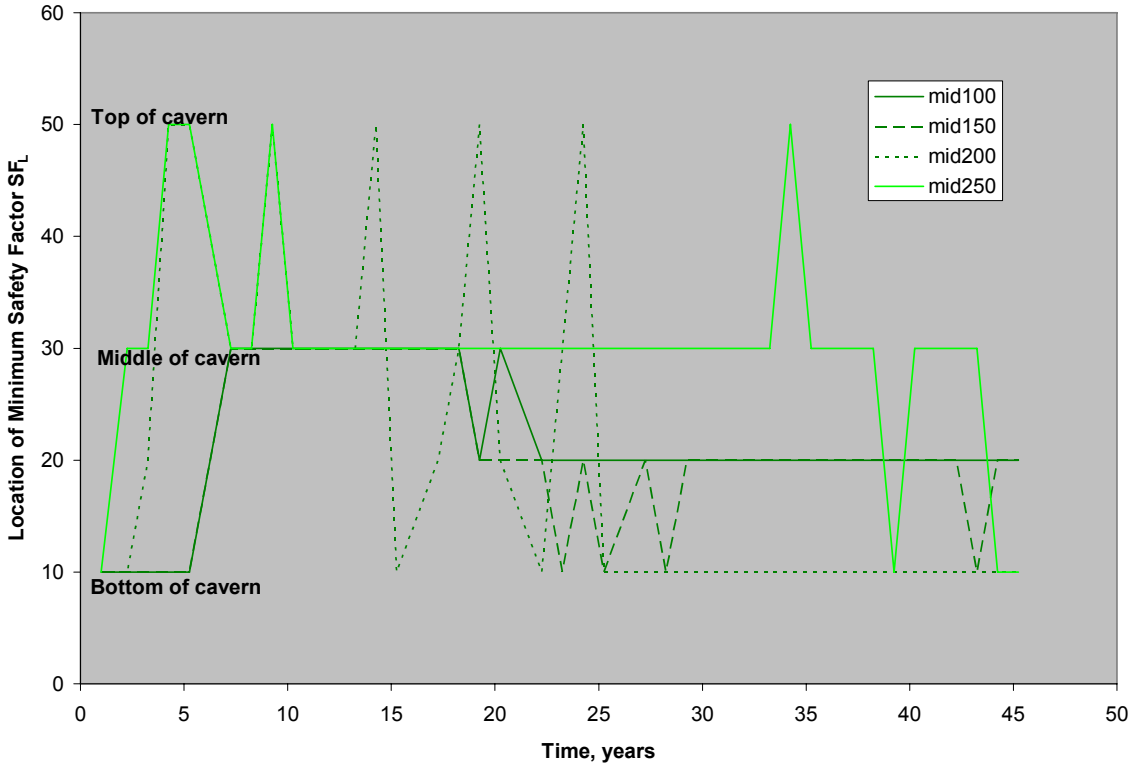

Figure 22. Location of minimum Lee safety factor, enlarged middle caverns.

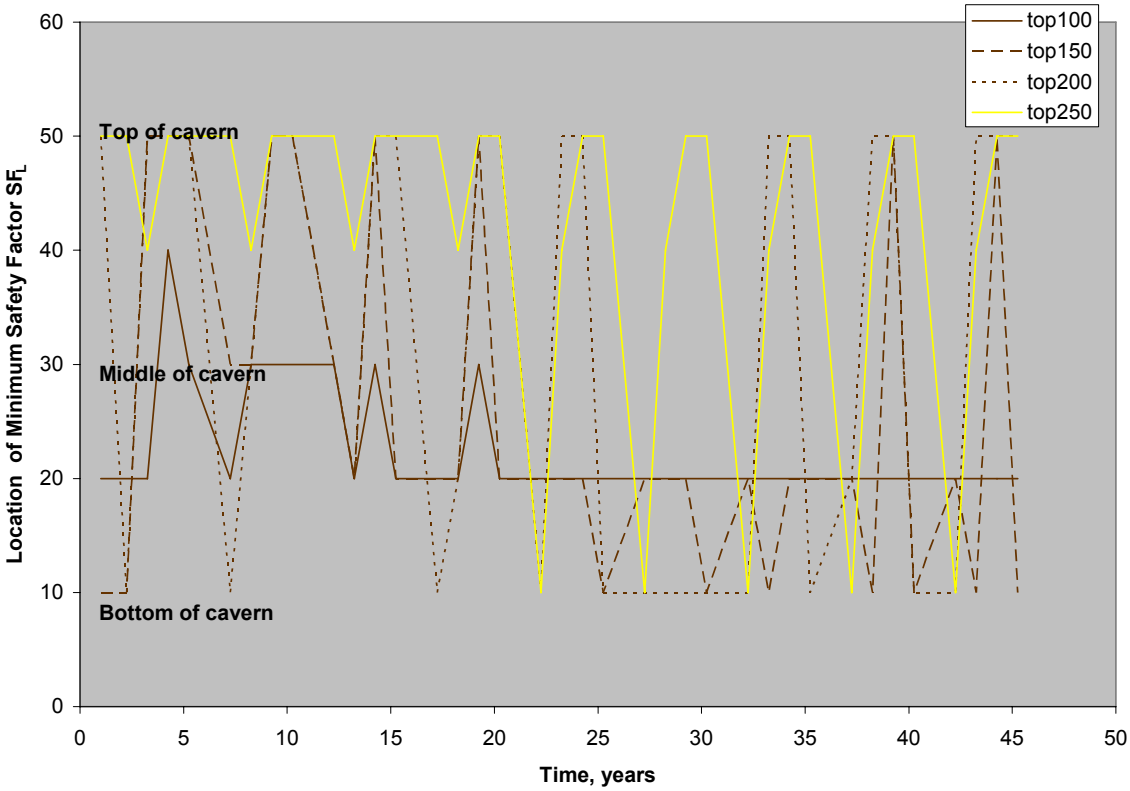

Figure 23. Location of minimum Lee safety factor, enlarged top caverns.

4.2 CAVERN VOLUME CLOSURE

The volume of the caverns decreases as the salts creeps. Figure 24 shows a history of the decrease in normalized volume for all seventeen cases. The normalized volume is the volume at a given time divided by the initial volume of each case before standard operations. The enlarged top caverns clearly exhibit the least cavern closure, and the enlarged bottom caverns clearly exhibit the greatest closure. An interesting observation that can be made is that the normalized cavern closure increases for the enlarged top case as the radius increases, but decreases for the other cases with increasing radius, with the exception that the closure suddenly increases from the 250-ft to the 300-ft-radius cylindrical caverns. This change for the cylindrical caverns at 300-ft radius indicates that the stress field around a cavern is no longer effectively independent, but is interacting with the stress field of the adjacent cavern. Remember that most of the intercavern web is much thicker than the P/D ratio. A more in-depth suite of calculations such as these should suggest the distance at which the cavern interaction causes accelerated closure. This effect of cavern shape and radius on closure is better illustrated in Figure 25, where the percent closure after 45 years of operation is plotted in terms of initial cavern volume. The enlarged top caverns have the least amount of cavern closure because both the downward displacement of the cavern ceiling and the upward displacement of the cavern floor are the least for the four design shapes. Similarly, the corresponding displacements for the enlarged bottom caverns are the greatest. The percent decrease in height for each cavern shape is shown in Figure 26. It seems counterintuitive that the enlarged top caverns would have the smallest downward ceiling displacement, as they have the largest area of oil pressure at the ceiling. However, the ΔP between oil pressure and in situ hydrostatic pressure at the top of the caverns is approximately 1100 psi, whereas the ΔP at the bottom of the caverns is about 2900 psi. Therefore, having the larger area at the bottom of the cavern allows the greater pressure difference there to dominate the overall redistribution of stress and deformation of the salt, thus producing in the cavern closure results shown here. A rank order, from best performance to worst, based on cavern volume closure would be: 1) enlarged top; 2&3) enlarged middle and cylinder; and 4) enlarged bottom.

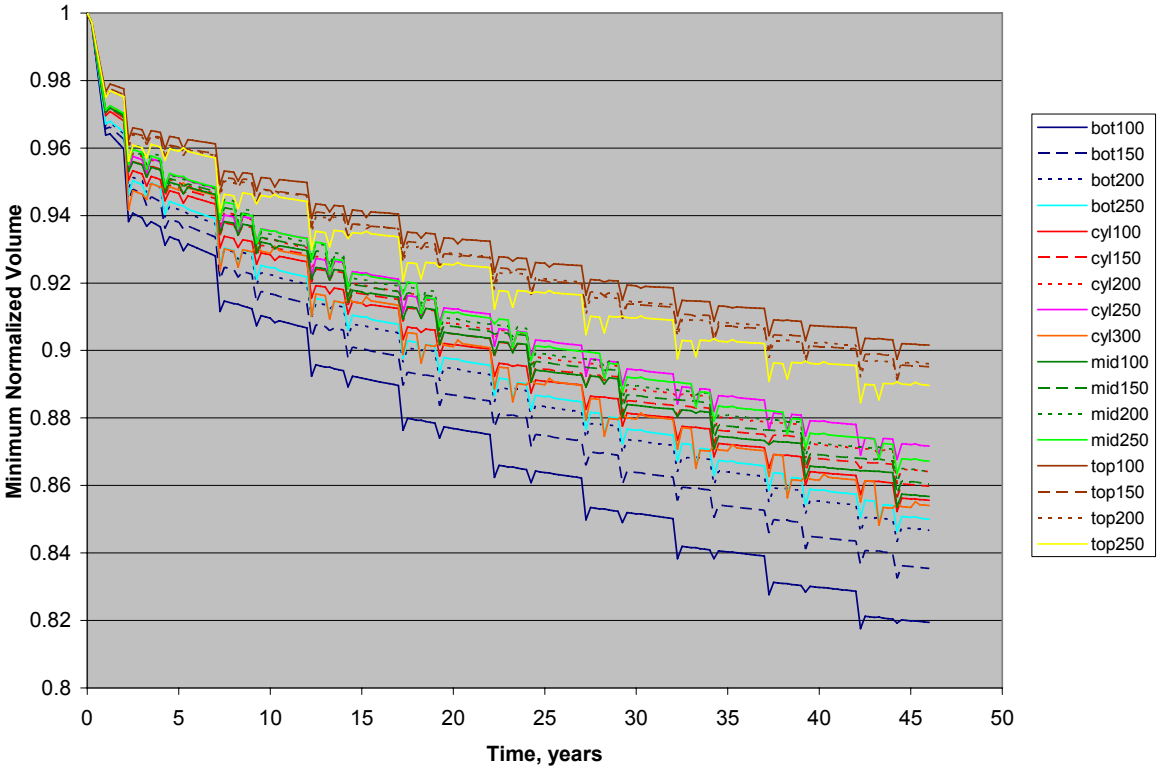

Figure 24. Minimum normalized volume history for all 17 cases.

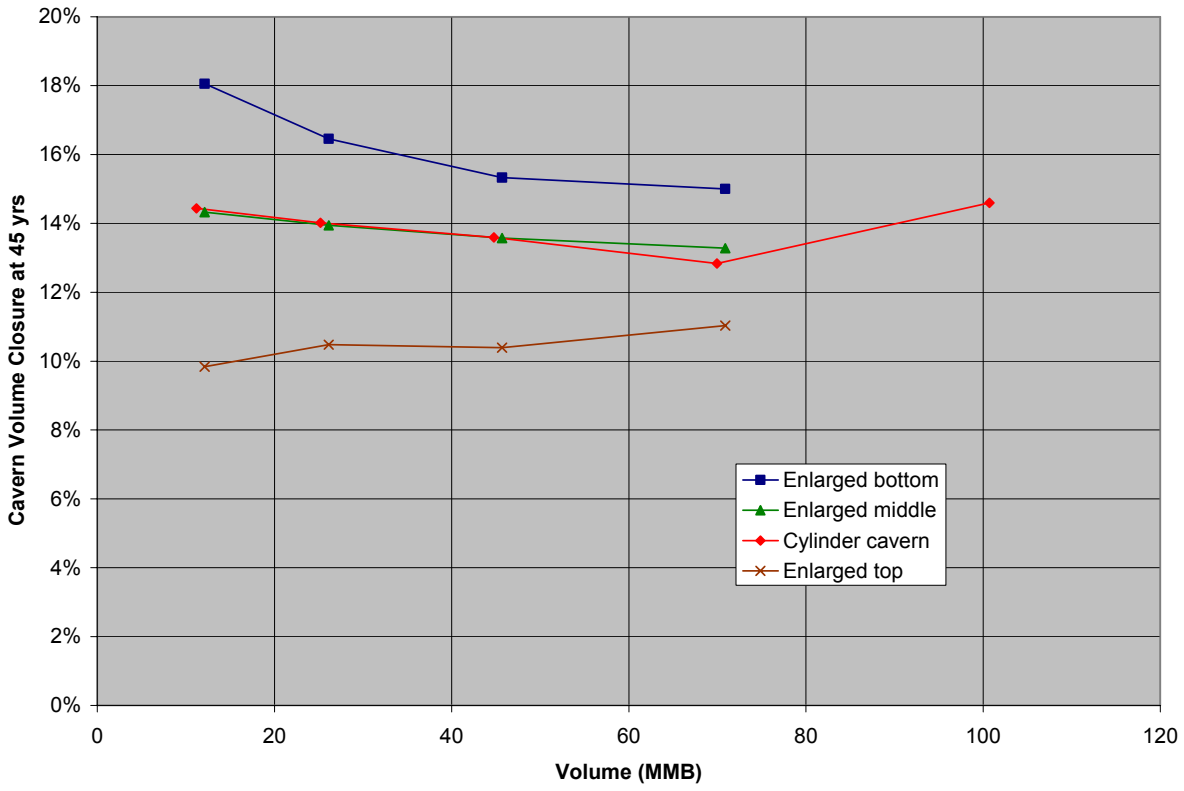

Figure 25. Cavern volume closure as a function of initial cavern volume.

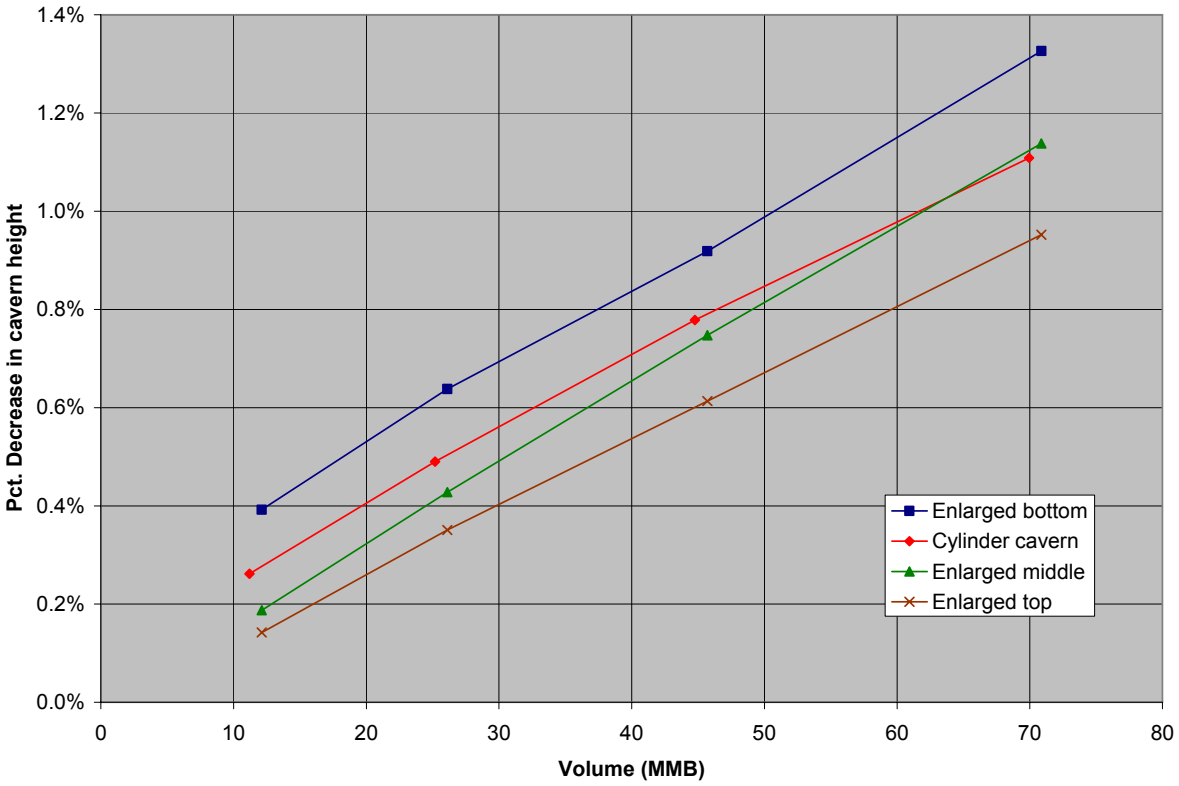

Figure 26. Decrease in cavern height as a function of initial cavern volume.

A further illustration of the cavern closure for each of the four shapes is shown in Figure 27, where vertical displacement is plotted for the final time step, and the initial cavern volume geometry is superimposed on the displacement contour plot. Several observations can be made from this plot. First, the magnitude of the vertical displacements is much higher for the enlarged bottom caverns, near 20m upward at the floor and nearly 3m downward near the ceiling. The line marking the change from negative to positive displacement is at nearly one-third the cavern height from the floor for the enlarged bottom, near the middle of the cavern for the cylindrical and enlarged middle caverns, and near the top for the enlarged top caverns. Also, note that the majority of salt deformation into the cavern space occurs from the floor and toward the middle of the cavern field. The larger displacements at the cavern floors result from the higher pressure differential between in situ hydrostatic and cavern operating pressures at the lower depths. The deformation toward the center of the cavern field is a natural result from creating several large cavities in a huge salt formation with substantial creep; the resulting horizontal deformations might be somewhat different and smaller in a field surrounded by a more elastic rock such as sandstone. This asymmetric cavern deformation pattern indicates the importance of three-dimensional calculations to properly determine the displacement and strain fields around caverns and in salt pillars.

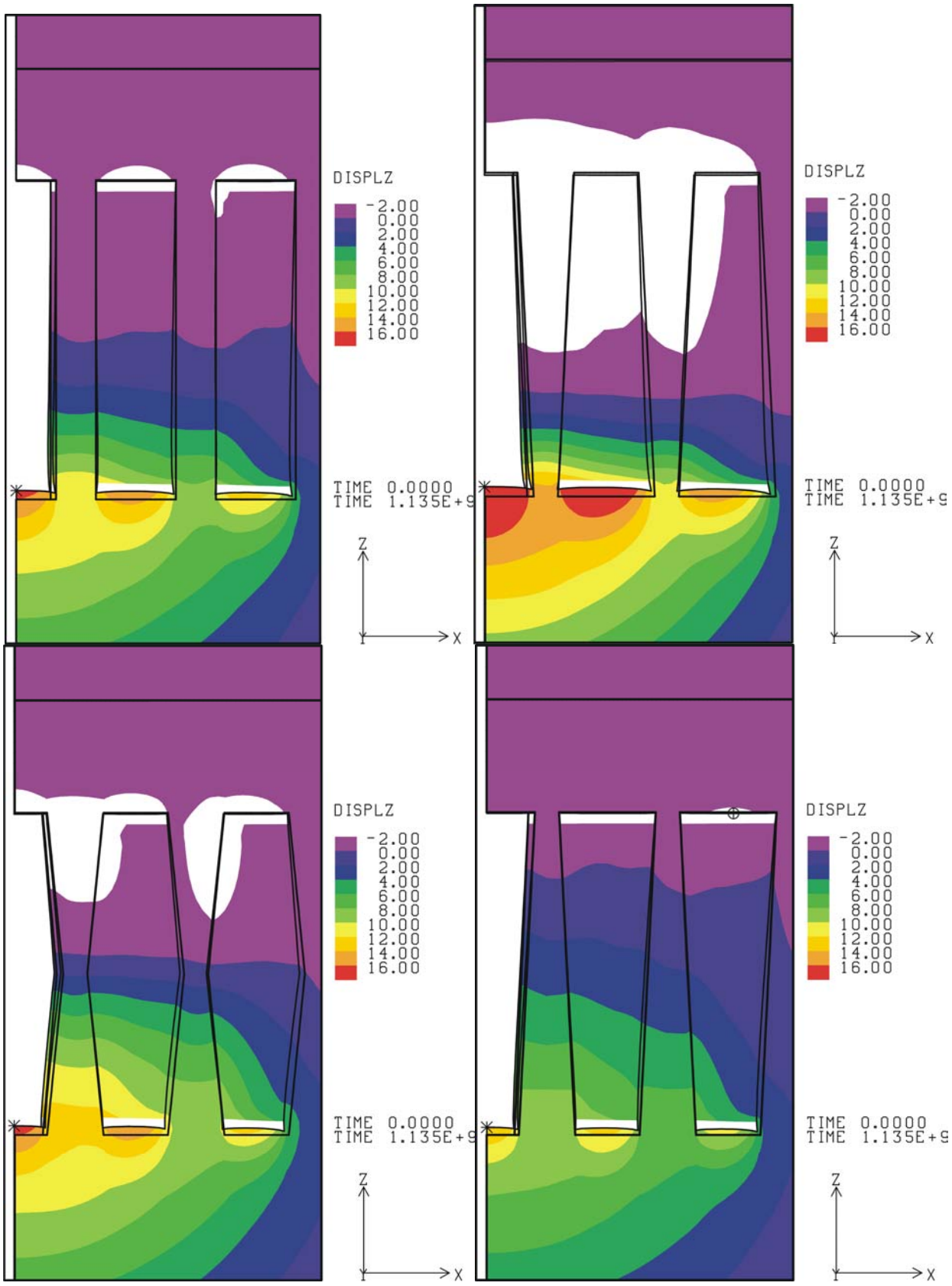

Figure 27. Contour plots of vertical displacement (displacements in meters).

4.3 AXIAL WELL STRAIN

The physical presence of wells and surface structures are not included in the finite element model, but the potential for ground deformation to damage these structures can be conservatively estimated by assuming that they will deform according to the predicted ground strains. At wells locations, subsidence will primarily induce elongation of the axis of the well. Under these conditions, the cemented annulus of the wells may crack forming a horizontal tensile fracture that may extend around the wellbore. This may not result in vertical fluid migration along the casing, but could permit horizontal infiltration into ground waters. This may be a vulnerability, especially in the caprock, where acidic ground waters may gain access to the steel casing and corrode it. More extensive damage could heavily fracture the cement which could result in a loss of well integrity in that leakage could occur from the cavern along the outside of the casing. Such leakage could result in flow to the surrounding environment, resulting in loss of product. The allowable axial strain for purposes of this report is assumed to be 0.2 millistrains in tension. This would be typical of cement with a compressive strength in the range from 2500 to 5000 psi (Thorton and Lew, 1983). It should also be noted that vertical well strain reduces the collapse resistance of the steel casings. For a typical SPR well located in the caprock, negligible casing collapse resistance is predicted at 1.6 millistrains.

A comparison of the predicted maximum axial strain of the well in the caprock after 45 years of operation for the 17 cases is shown in Figure 28. Note that the enlarged top caverns have the least axial well strain of the four shapes, due in large part to the lesser amount of downward displacement of the ceiling of the caverns discussed in the previous section. Similarly, the enlarged bottom caverns produce the greatest axial strains. Figure 29 presents the same comparison as a function of average P/D ratio, with similar comparative results. A rank order, from best performance to worst, based on axial well strain in the caprock would be: 1) enlarged top; 2) cylinder; 3) enlarged middle; and 4) enlarged bottom.

Figures 28 and 29 indicate that all cavern shapes will eventually cause well strains over 0.2 millstrains as the initial cavern (cavern volume) radius increases. Note that factors other than cavern shape, including depth of wellbore, thickness of the various geological layers, and cohesion of the steel and cement to the surrounding sand, salt, and rocks, also influence the axial strain imparted to the well casings. Therefore, the plots in Figures 28 and 29 are meant to be used as a comparison between cavern shapes. A more specific analysis of well casing behavior can be found in Sobolik and Ehgartner (2006), and similar studies would be suggested for site-specific geological conditions.

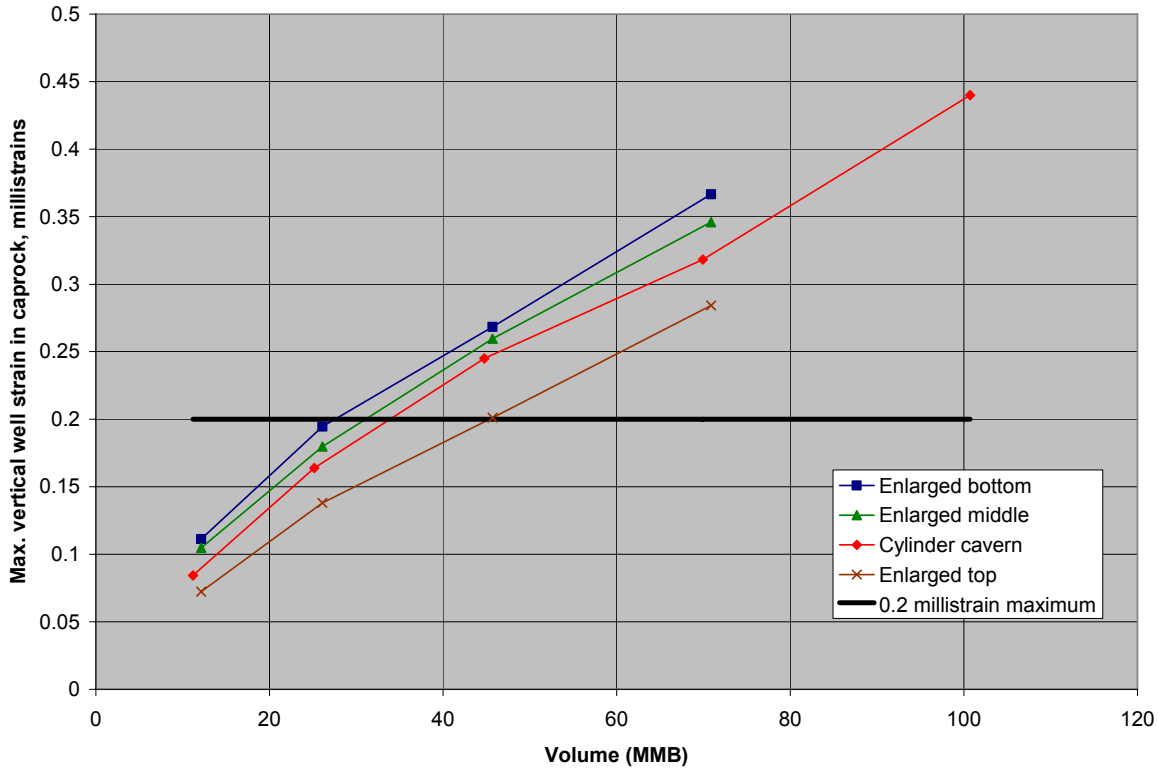

Figure 28. Maximum vertical well strain in caprock as a function of initial cavern volume.

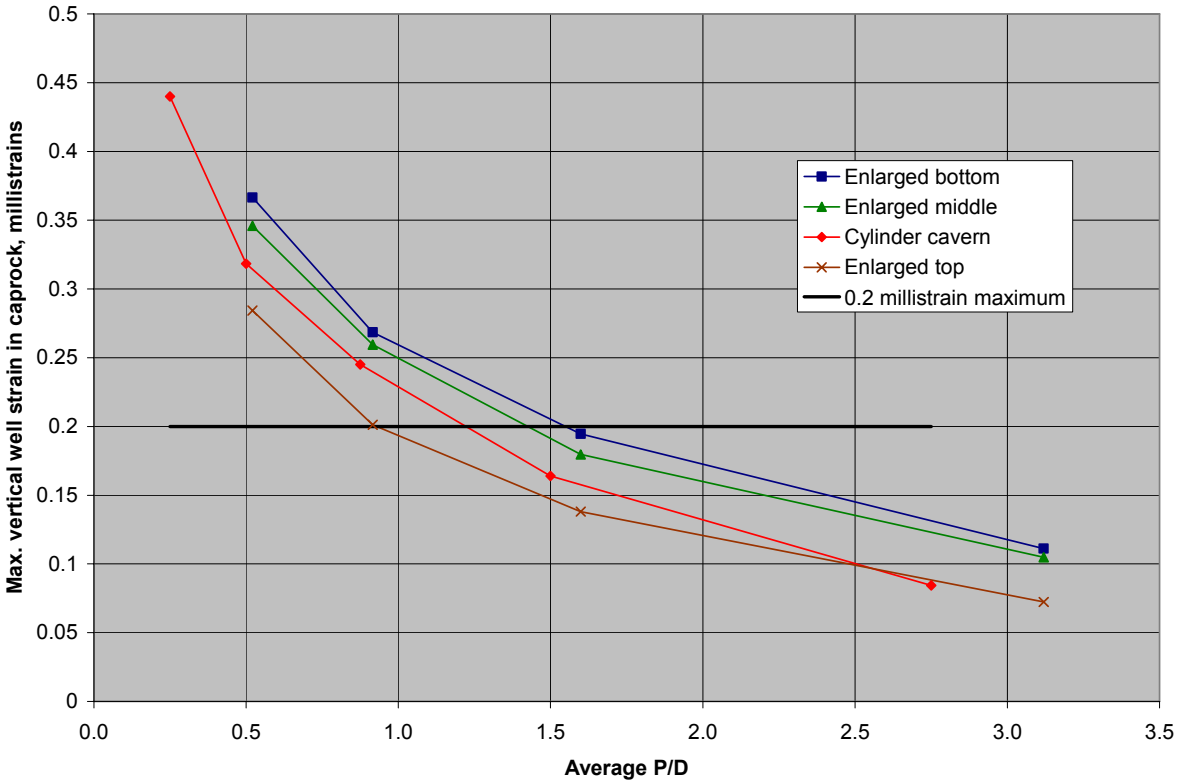

Figure 29. Maximum vertical well strain in caprock as a function of average P/D ratio.

4.4 SURFACE SUBSIDENCE

The issue of surface subsidence is an important design and operations factor for surface facilities, especially for those located in flood prone areas, but subsidence also results in horizontal ground strains that can damage buildings, pipelines, and other infrastrusture. Expected subsidence during the 100-year life of a facility on the order of up to ten feet is not uncommon. Therefore, the performance of a cavern shape design can be defined by the expected subsidence. Figures 30 and 31 compare the predicted surface subsidence of the 17 cases as a function of initial cavern volume and average P/D ratio, respectively. Because of the lesser amount to cavern deformation predicted for the enlarged top design, the surface subsidence for that case is also predicted to be the least. The enlarged bottom caverns are predicted to produce 60-70% more surface subsidence than the enlarged top caverns. The enlarged middle and cylindrical designs produce similar results to each other. A rank order, from best performance to worst, based on surface subsidence would be: 1) enlarged top; 2) cylinder; 3) enlarged middle; and 4) enlarged bottom.

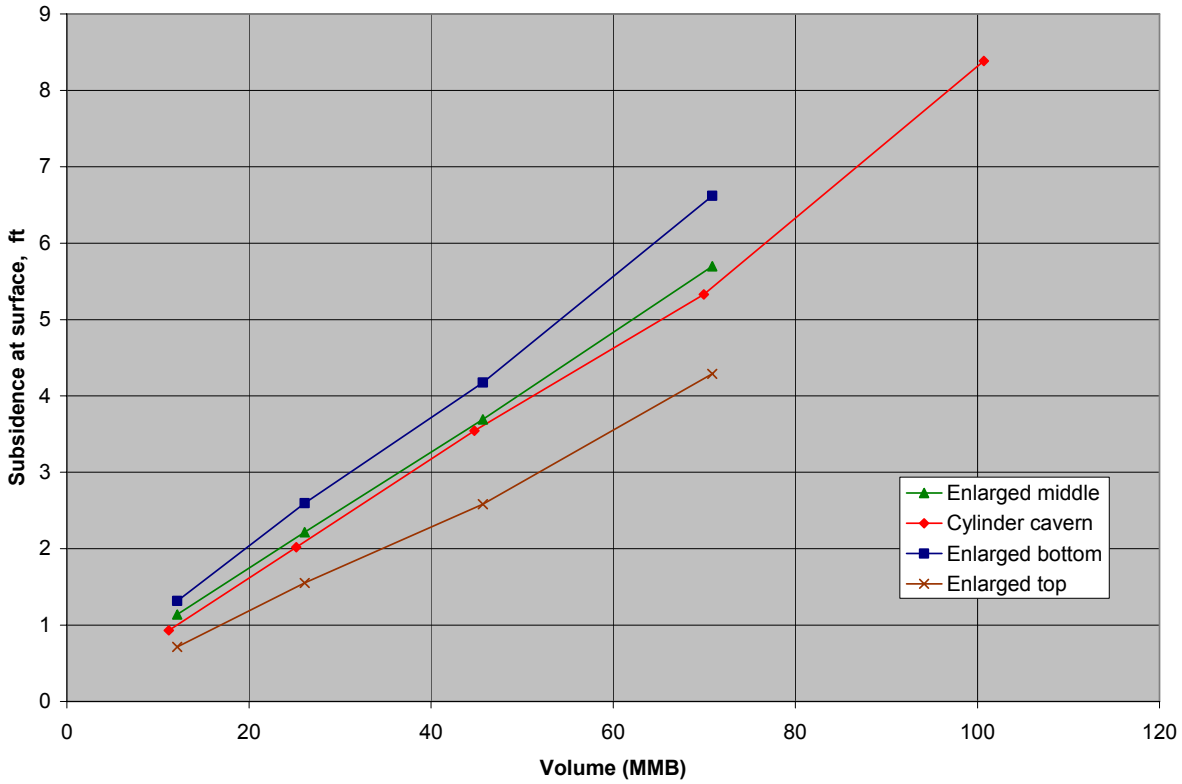

Figure 30. Maximum surface subsidence as a function of initial cavern volume.

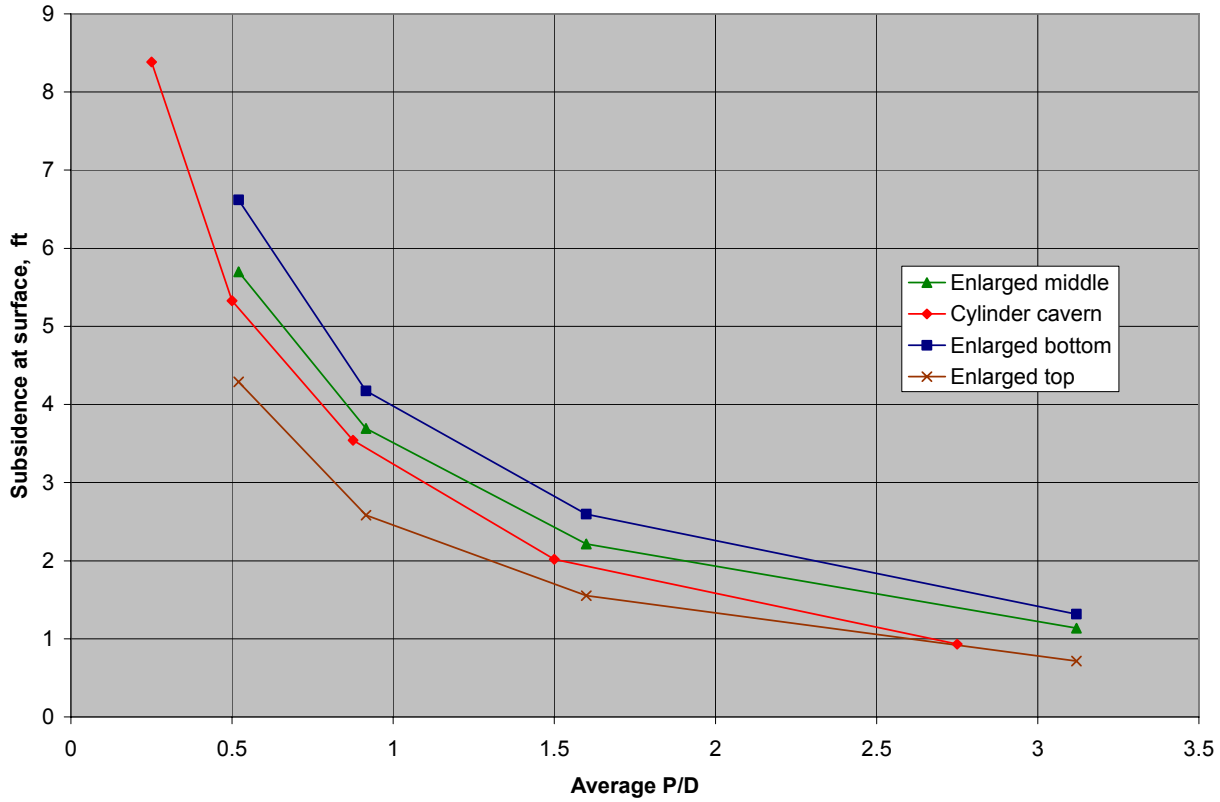

Figure 31. Maximum surface subsidence as a function of average P/D ratio.

Structural damage on the surface is typically caused by large accumulated surface strains caused by surface subsidence. These strains can cause distortion, damage, and failure of buildings, pipelines, roads, bridges, and other infrastructure. Surface strains will accumulate in structures over time, which increases the possibility of damage in older facilities. Typically, subsidence strains tend to be compressive in the central portion of the subsided area and become tensile in nature for areas farther removed. Some guidance and solutions are available to evaluate the predicted surface strains. These criteria vary from country to country, possibly due to different building codes and structural materials. Some examples of allowable strains are presented by Peng (1985). The criteria vary in some countries depending on application. For purposes of this paper, the allowable strain is taken to be 1 millistrain for both compression and tension. Criteria for shear strains have not been found, perhaps because they are less important. In practice, allowable strain limits for a structure are design specific and should be examined on a case-by-case basis.

The horizontal surface strains are related to the subsidence above the caverns. Typically, the region above the caverns undergo compressive horizontal stresses at the surface as the geologic units sag, but at some distance away from the cavern field the horizontal strains become tensile at the periphery of the subsidence trough or depression. Figures 32 and 33 show the predicted maximum horizontal compressive and tensile ground strains for the 17 cases. Note the similarity of these curves to those for surface subsidence showing the enlarged bottom case as the worse condition. The maximum compressive strain occurs directly over the center cavern

(Cavern 1), whereas the maximum tensile strain occurs at a radius ranging from 4800-6500 ft from the center cavern, with this distance increasing as the cavern radii increase. The surface strains for the enlarged bottom cavern (bot 250) are shown in Figure 34 at 45 years. In all cases, the predicted maximum strains are below the threshold 1 millistrain, but as discussed above the predicted ground strains will vary by site due to the geology and specifics of the cavern field.

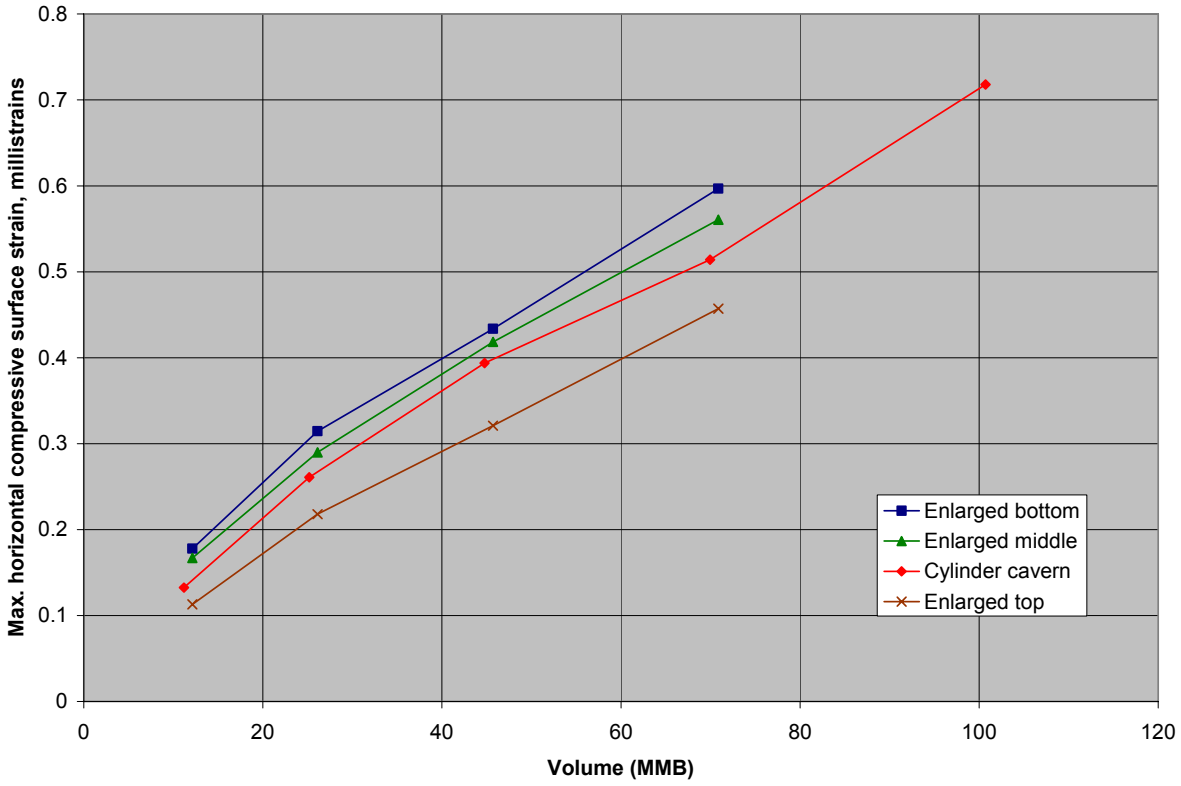

Figure 32. Predicted Maximum Compressive Ground Strains at Surface.

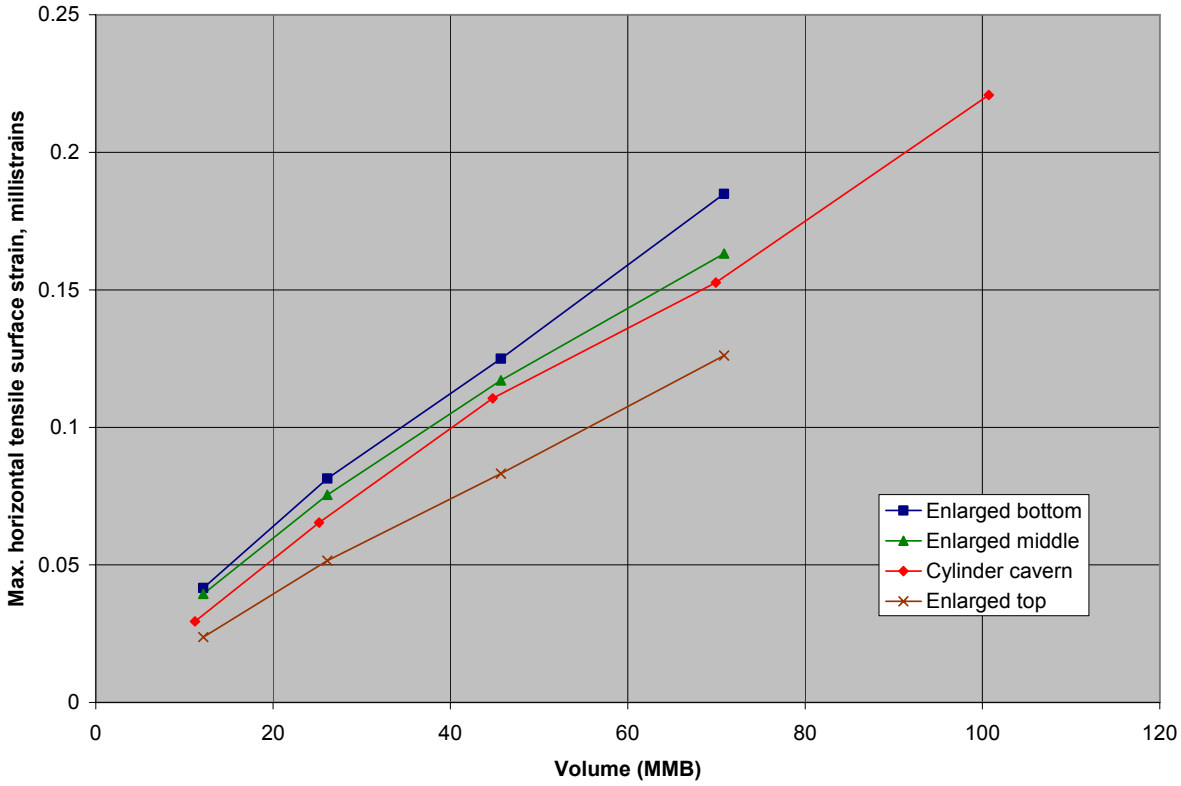

Figure 33. Predicted Maximum Tensile Ground Strains at Surface.

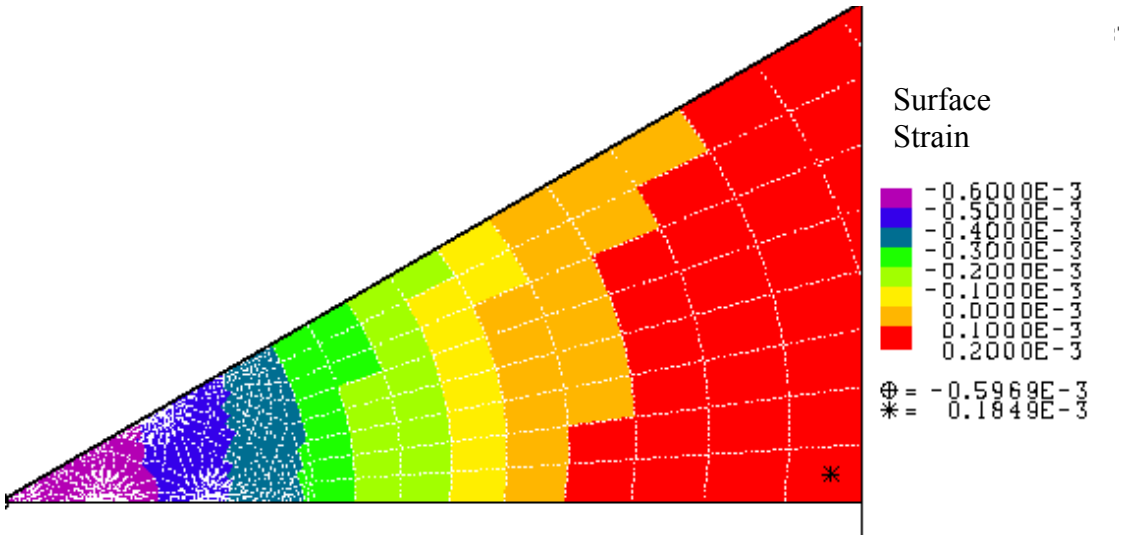

Figure 34. Distribution of Compressive (-) and Tensile (+) Surface Ground Strains at 45 Years.

4.5 SUMMARY OF CAVERN SHAPE RANKINGS

Table 7 provides a summary of the rankings of the performance of the four cavern shapes based on the four design factors. The enlarged top caverns appear to produce the least amount of geological deformation, as measured by cavern volume closure, axial well strain, and surface

subsidence. This minimal amount of deformation is likely due to the fact that the enlarged top (and therefore, tapered bottom) has less cavern surface area in the region of highest pressure differential between oil pressure and in situ hydrostatic pressure, at the bottom of the caverns, decreasing upward vertical displacement of the floor. Also, the angle of the slope of the cavern walls allow for an effective uplift force, decreasing downward vertical displacement of the ceiling. However, this decrease in deformation comes at the price of higher deviatoric stresses, making the possibility of dilatant damage and fracturing greater in the roof than for the other cases. The enlarged bottom caverns appear to have the least overall desired features, and the enlarged middle caverns have some of the advantages of the enlarged top caverns with lesser deviatoric stresses.

Table 7. Summary of cavern shape rankings.

Design Factor	1st	2nd	3rd	4th
Safety factor in salt	enlarged middle	enlarged bottom	cylinder	enlarged top
Cavern volume closure	enlarged top	enlarged middle, cylinder		enlarged bottom
Axial well strain	enlarged top	cylinder	enlarged middle	enlarged bottom
Surface subsidence	enlarged top	cylinder	enlarged middle	enlarged bottom

5. CONCLUSIONS

These analyses evaluated the effect of cavern shape on the performance and stability of underground reservoirs in salt domes. Four cavern shapes – cylindrical, enlarged top, enlarged middle, and enlarged bottom – were evaluated against four design factors. These factors included the dilatant damage safety factor in salt, the cavern volume closure, axial well strain in the caprock, and surface subsidence. The following conclusions were obtained from the results of the analyses:

- The enlarged top caverns had the best performance when evaluated against the design factor of cavern volume closure, axial well strain in the caprock, and surface subsidence. This performance was caused by the minimization of cavern surface area in the deeper regions where the pressure differential between in situ hydrostatic pressure and operating oil pressure is greatest, and also by the direction of force created by the angle of the cavern walls, directing the pressure differential to hold up the cavern ceiling. This performance comes at the expense of the greater possibility for dilatant or shear damage, for which the enlarged top caverns performed the worst.
- The enlarged middle design has the highest safety factors of the four designs, and was in the middle of the group for the other three design factors.
- The enlarged bottom caverns had generally the worst performance of the four designs.
- The average P/D ratio provides a more realistic comparison parameter for the different cavern shapes than the minimum P/D ratio.

The results of this study are applicable to existing cavern geometries and are also useful in evaluating behavior of future cavern shapes due to leaching associated with oil drawdowns and cavern shapes under consideration for expansion of the SPR. The results also show the sensitivity of important cavern performance measures as caverns deviate from the commonly simulated or assumed cylindrical cavern shape. The findings of this study are cast in terms of cavern volume for application in designing new cavern fields, and in terms of the pillar to diameter ratio which is commonly used to evaluate stability of existing caverns. Future analyses could examine the impact of the geology, particularly the caprock, on the performance metrics and consider even greater distortions in cavern shape, particularly with respect to the enlarged mid-section which was shown to provide a favorable cavern shape and the enlarged roof caverns. Further analyses of those cavern shapes could define optimal cavern shapes.

6. REFERENCES

- Blanford, M.L., M.W. Heinstein, and S.W. Key, 2001. *JAS3D. A Multi-Strategy Iterative Code for Solid Mechanics Analysis.* ***User's Instructions****, Release 2.0*. SEACAS Library, JAS3D Manuals, Computational Solid Mechanics / Structural Dynamics, Sandia National Laboratories, Albuquerque, NM.
- Butcher, B.M., 1997. *A Summary of the Sources of Input Parameter Values for the WIPP Final Porosity Surface Calculations*, SAND97-0796 Sandia National Laboratories, Albuquerque, NM.
- DOE (U.S. Department of Energy), 2001. Design Criteria- Level III. US Department of Energy, Strategic Petroleum Reserve, New Orleans, LA, November, 2001.
- Ehgartner, B.L., S.J. Bauer, and D.E. Munson, 2002. Big Hill Salt Strength, Draft Report to Robert E. Myers, DOE SPR PMO FE-4421, November 18, 2002.
- Ehgartner, B.L. and S.R. Sobolik, 2002. *3-D Cavern Enlargement Analyses*, SAND2002-0526, Sandia National Laboratories, Albuquerque, NM.
- Hoffman, E.L. and B.L. Ehgartner, 1993. *Evaluating the Effects of the Number of Caverns on the Performance of Underground Oil Storage Facilities*, Int. J. Rock Mech. Min. Sci. & Geomech. Abstr. Vol. 30, No. 7, pp. 1523-1526.
- Hugout, B., E. Chaudan, and M. Dussaud, 1988. *Influence of Creep on Shape of Salt Cavities of Natural Gas Storage*, Spring Meeting, Solution Mining Research Institute, Mobile, AL.
- Krieg, R.D., 1984. *Reference Stratigraphy and Rock Properties for the Waste Isolation Pilot Plant (WIPP) Project*, SAND83-1908, Sandia National Laboratories, Albuquerque, NM.
- Lee, M.Y., B.L. Ehgartner, B.Y. Park, and D.R. Bronowski, 2004. *Laboratory Evaluation of Damage Criteria and Permeability of Big Hill Salt*, SAND2004-6004, Sandia National Laboratories, Albuquerque, NM.
- Levin, B.L., Impact Study of Big Hill Draw Down Scenarios on Cavern Integrity. Letter Report to Wayne Elias, September 27, 2004.
- Magorian, T.R, and J.T. Neal, 1988. *Strategic Petroleum Reserve (SPR) Addition Geological Site Characterization Studies Big Hill Salt Dome, Texas*, SAND88-2267, Sandia National Laboratories**,** Albuquerque, NM.
- Morgan, H.S. and R.D. Krieg, 1990. *Investigation of an Empirical Creep Law for Rock Salt that Uses Reduced Elastic Moduli*, SAND89-2322C, presented at the 31st U.S. Symposium on Rock Mechanics held in the CO School of Mines in June 18-20, 1990, Sandia National Laboratories, Albuquerque, NM.
- Munson, D.E., 1998. *Analysis of Multistage and Other Creep Data for Domal Salts*, SAND98-2276, Sandia National Laboratories, Albuquerque, NM.
- Neal, J.T., T.R. Magorian, K.O. Byrne, and S. Denzler, 1993. *Strategic Petroleum Reserve (SPR) Additional Geologic Site Characterization Studies Bayou Choctaw Salt Dome, Louisiana*, SAND92-2284, Sandia National Laboratories, Albuquerque, NM.
- Park, B.Y., B.L. Ehgartner, M.Y. Lee, and S.R. Sobolik, 2005. *Three Dimensional Simulation for Big Hill Strategic Petroleum Reserve (SPR)*, SAND2005-3216, Sandia National Laboratories, Albuquerque, NM.

- PB-KBB Inc., 1978. Strategic Petroleum Reserve Program, Salt Dome Geology and Cavern Stability Analysis, Bayou Choctaw Dome, Louisiana, Final Report, Appendix, Prepared for U.S. Department of Energy, Houston, TX.
- Peng, S.S., 1985. Coal Mine Ground Control. 2nd Ed., John Wiley and Sons, New York NY.
- Preece, D.S., and W.R. Wawersik, 1984. Leached Salt Cavern Design Using a Fracture Criterion for Rock Salt, SAND83-2345C, presented at the 25th U.S. Symposium on Rock Mechanics held at Northwestern University in Evanston, IL in June 25-27, 1984, Sandia National Laboratories, Albuquerque, NM.
- Price, R.H., W.R. Wawersik, O.W. Hannum, and J.A. Zirzow, 1981. *Quasi-Static Rock Mechanics Data for Rocksalt from Three Strategic Petroleum Reserve Domes*, SAND81-2521, Sandia National Laboratories, Albuquerque, NM.
- Rautman, C., et al., 2005. An Updated Three-Dimensional Site Characterization Model of the Big Hill Strategic Petroleum Reserve Site, Texas, Sandia National Laboratories, Albuquerque, NM, Draft of SAND report dated January 5, 2005.
- Sobolik, S.R. and B.L. Ehgartner, 2006. *Analysis of Salt and Casing Fracture Mechanisms During Cavern Integrity Testing for SPR Salt Caverns*, SAND2006-1974, Sandia National Laboratories, Albuquerque, New Mexico.
- Stein, J.S., 2005a. Working version of 3-D 'pillar-to-diameter' code and demonstration of application to two SPR sites with irregular spacing. Letter Report to Wayne Elias, February 15, 2005.
- Stein, J.S., 2005b. Possibilities for placing new SPR caverns in the Sabine Pass Terminal at the Big Hill SPR site. Letter Report to Wayne Elias, June 20, 2005.
- Thorton, C.H and I.P. Lew, 1983. *Concrete and Design Construction. Standard Handbook for Civil Engineers*, Chapter 8, 3rd ed., F.S. Merritt, editor, McGraw-Hill, New York, NY.
- Van Sambeek, L.L., J.L. Ratigan, and F.D. Hansen, 1993. *Dilatancy of Rock Salt in Laboratory Tests*, Int. J. Rock Mech. Min. Sci. & Geomech. Abstr. Vol. 30, No. 7, pp 735-738.
- Wawersik, W.R. and D.H. Zeuch, 1984. *Creep and Creep Modeling of Three Domal Salts – A Comprehensive Update*, SAND84-0568, Sandia National Laboratories, Albuquerque, NM.

DISTRIBUTION:

5	MS	0706	D. J. Borns, 6113
5	MS	0706	B. L. Ehgartner, 6113
5	MS	0751	T. W. Pfeifle, 6117
5	MS	0751	S. R. Sobolik, 6117
1	MS	0751	M. Y. Lee, 6117
1	MS	1395	B. Y. Park, 6821
1	MS	0701	P. B. Davies, 6100
1	MS	0701	J. A. Merson, 6110
1	MS	0735	R. E. Finley, 6115
1	MS	0376	J. G. Arguello, 1526
1	MS	0376	C. M. Stone, 1527
2	MS	9018	Central Technical Files, 8944
2	MS	0899	Technical Library, 4536

Electronic copy only to Wayne Elias at Elias.Wayne@SPR.DOE.GOV for distribution to DOE and DM